Assessing spatial and temporal variability of phytoplankton communities' composition in the Iroise Sea ecosystem (Brittany, France): A 3D modeling approach. Part 1: Biophysical control over plankton functional types succession and distribution

Mathilde Cadier [a,*], Thomas Gorgues [b], Marc Sourisseau [c], Christopher A. Edwards [d], Olivier Aumont [e], Louis Marié [b], Laurent Memery [a]

[a] Laboratoire des Sciences de l'Environnement Marin (LEMAR), UMR CNRS/IFREMER/IRD/UBO 6539, 29280 Plouzané, France
[b] Laboratoire d'Océanographie Physique et Spatiale (LOPS), Univ. Brest, CNRS, IRD, Ifremer, IUEM, 29280 Plouzané, France
[c] Département Dynamiques de l'Environnement Côtier (DYNECO)/PELAGOS, Ifremer Centre de Brest, 29280 Plouzané, France
[d] Institute of Marine Sciences, University of California, Santa Cruz, CA 95064, USA
[e] Laboratoire d'Océanographie et du Climat: Expérimentations et Approches Numériques (LOCEAN), 75005 Paris, France

ARTICLE INFO

ABSTRACT

Understanding the dynamic interplay between physical, biogeochemical and biological processes represents a key challenge in oceanography, particularly in shelf seas where complex hydrodynamics are likely to drive nutrient distribution and niche partitioning of phytoplankton communities. The Iroise Sea includes a tidal front called the 'Ushant Front' that undergoes a pronounced seasonal cycle, with a marked signal during the summer. These characteristics as well as relatively good observational sampling make it a region of choice to study processes impacting phytoplankton dynamics. This innovative modeling study employs a phytoplankton-diversity model, coupled to a regional circulation model to explore mechanisms that alter biogeography of phytoplankton in this highly dynamic environment. Phytoplankton assemblages are mainly influenced by the depth of the mixed layer on a seasonal time scale. Indeed, solar incident irradiance is a limiting resource for phototrophic growth and small phytoplankton cells are advantaged over larger cells. This phenomenon is particularly relevant when vertical mixing is intense, such as during winter and early spring. Relaxation of wind-induced mixing in April causes an improvement of irradiance experienced by cells across the whole study area. This leads, in late spring, to a competitive advantage of larger functional groups such as diatoms as long as the nutrient supply is sufficient. This dominance of large, fast-growing autotrophic cells is also maintained during summer in the productive tidally-mixed shelf waters. In the oligotrophic surface layer of the western part of the Iroise Sea, small cells coexist in a greater proportion with large, nutrient limited cells. The productive Ushant tidal front's region (1800 mgC·m^{-2}·d^{-1} between August and September) is also characterized by a high degree of coexistence between three functional groups (diatoms, micro/nano-flagellates and small eukaryotes/cyanobacteria). Consistent with previous studies, the biogeography of phytoplankton functional types at the Ushant front during summer displays an intermediate community composition between contrasted sub-regions on either side of the front. Strong mixing conditions within the frontal sub-region result in a short residence time of water masses, not allowing speciation or long term adaptation to occur.

© 2016 Published by Elsevier B.V.

1. Introduction

Temperate coastal areas are highly productive systems which support complex trophic networks. Understanding these coveted ecosystems with particular interests such as fisheries, aquaculture, and marine protected areas, is valuable for their sustainable management. Dynamic physical features (*e.g.* submesoscale structures, filaments and fronts) impact coastal ecosystems making them highly heterogeneous areas and hosting very diverse communities of species. Hydrodynamic variability through time and space results in various ecological niches occupied by different primary producer communities whose physiological characteristics (*e.g.* life-history traits) are mainly driven by light and/or nutrient availability together with predation pressure by grazers (Margalef, 1978).

Among heterogeneous coastal environments, the Iroise Sea is one of the major tidal front ecosystems in the world. Located along the western coast of France (North-East Atlantic) (Fig. 1A), this shelf sea exhibits a strong seasonal cycle driven by the interplay between atmospheric forcing and tidal currents over the shallow sea floor above the continental shelf (Le Fèvre and Grall, 1970; Mariette et al., 1982). During the summer season (May to October), the Ushant tidal front separates thermally stratified oceanic waters to its west from homogeneous, tidally mixed waters near the coast (Le Fèvre et al., 1983; Mariette and Le Cann, 1985). This hydrographic structure has been explored extensively for its strong influence on the Iroise Sea ecosystem, both in terms of physical properties and biological features. At the front location, horizontal density gradients at the surface and bottom are in opposite direction, inducing geostrophic instabilities, strong cross-frontal currents and cyclonic eddies with a few days lifetime (Pingree, 1978). As is typical for tidal front regions (Franks, 1992; Holligan et al., 1984), a well-established phytoplankton bloom is observed at the Ushant front location during this period (Le Corre and L'Helguen, 1993).

In terms of community composition, diatoms have been shown to be the most abundant photosynthetic organisms in the well-mixed waters (east of the front), whereas small flagellates are dominant in the oligotrophic surface waters to the west. In the latter region, a sub-surface chlorophyll maximum exists and comprises a mixture of diatoms and dinoflagellates that are also found in large proportions in the frontal area (Pingree et al., 1978).

Recently, several field programs (FroMVar cruises) have produced a more complete description of the frontal structure and residual circulation during the string/neap tide cycle (Le Boyer et al., 2009). Using an imaging method (Video-Fluorescence analyzer) method, Landeira et al. (2014) proposed to relate the abundance and size of phytoplankton (predominantly chain-forming diatoms) to physical properties (e.g. vertical mixing) in the Ushant front area. Their encouraging results showed plasticity in the length of diatom chains following changes in turbulence and vertical nitrate fluxes. Compared to neap tide conditions, the spring tide conditions seem to favor longer (although less numerous) chains.

The highly dynamic behavior and spatial heterogeneity of the Ushant front environment, combined with a good knowledge of physical processes in the region, make the Iroise Sea ecosystem particularly suitable for a modeling study of the influence of biophysical interactions on the phytoplankton communities' structure.

In this context, the aim of this paper is to provide a complementary, numerical approach to better understand the spatial and temporal variations of the Iroise sea/Ushant front biogeochemical and ecological characteristics in relation to physical properties over a seasonal cycle. This study is the first realistic biogeochemical modeling exercise focusing on this region (i.e. observational data of various origins are used to validate the simulations). Particular attention is placed on the identification and understanding of physical and biological processes through which successions and spatial distributions of major phytoplankton groups occur in this highly dynamic, seasonally variable tidal environment.

More precisely, the main scientific questions addressed in this study are (i) how are phytoplankton communities driven by hydrodynamical properties of the Iroise Sea water masses over a seasonal cycle? and (ii) what is the influence of the frontal area on ecosystem properties (e.g. phototrophic biomass, primary production and plankton functional groups distribution)?

To address these questions, we use the phytoplankton-diversity model DARWIN, which accounts for a large number of phytoplankton phenotypes (Follows et al., 2007). The present study, which concerns mainly the bioregionalisation of the functional diversity, is the first of two papers; the second addresses diversity within the various functional groups (i.e. phenotypic diversity) (Cadier et al., subm.). Moreover, the DARWIN model allows the simulation of phytoplankton's broad range of growth strategies (phenotypes) within functional groups. The whole emerging community is then selected through environmental pressure. Contrary to classic 'plankton functional types' models, DARWIN thus minimizes the number of assumptions constraining model parameters as it does not require the choice of unique growth parameters values in each functional group.

2. Material and methods

2.1. Model formulations

To characterize the seasonal and spatial variations of dominant biogeochemical properties and ecological processes (i.e. competition and selection within the phytoplankton communities), a coupled physical/ecosystem model using the ROMS (Regional Ocean Modeling System) circulation model (Shchepetkin and McWilliams, 2005) and a
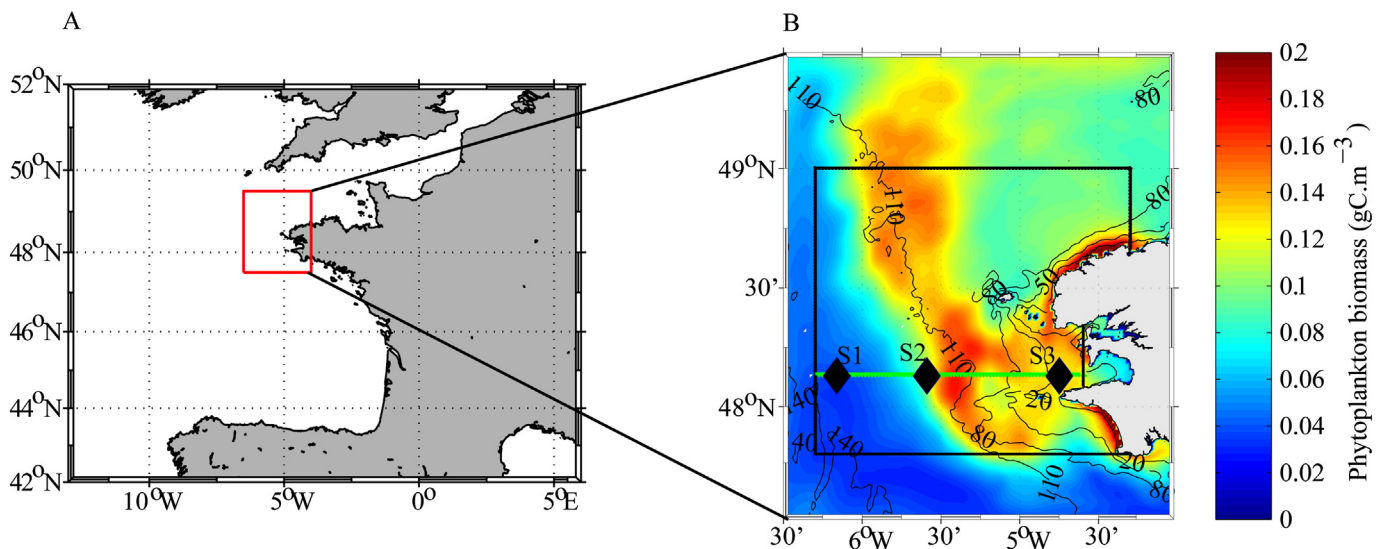

Fig. 1. Location of the study area. (A) Position of the Iroise Sea in the North East Atlantic Ocean (France). Modeling area's exact boundaries are defined by the red box. (B) Bathymetry (m) (black contours) over the surface total phytoplankton concentrations simulated by the model during summer (August–September average). The zonal section used in Figs. 4–8 (vertical sections) and Figs. 9 and 12 (Hovmöller diagrams) is drawn in green. Stations 1 to 3 used in Figs. 5 and 16 are plot by black diamonds. The black box is the contour of the study area used to compute diagnostics and following figures. (For interpretation of the references to color in this figure legend, the reader is referred to the web version of this article.)

'plankton-diversity' based model (DARWIN) derived from Follows et al. (2007) have been employed. The biogeochemical model is run online with the physical model with a common short time step of 100 s.

2.1.1. Physical model configuration

The IRD-INRIA version of the Regional Ocean Modeling system (ROMS-AGRIF (Penven et al., 2006)) is applied to the Iroise Sea to simulate its general circulation and physical features. ROMS-AGRIF is a split-explicit, free-surface oceanic model. Several factors make this circulation model highly suitable for coastal/regional applications: (i) terrain-following, curvilinear vertical coordinates, (ii) high order lateral advection schemes (third-order upstream-biased scheme for momentum, temperature and salinity and a Weighted-Essentially-Non-Oscillatory fifth-order scheme (Liu et al., 1994; Jiang and Shu, 1996) for biogeochemical tracers), and (iii) a high performance mixing/turbulence closure scheme (non-local, K-Profile planetary (KPP) boundary layer scheme (Large et al., 1994)). In the present study, our model configuration has 30 vertical sigma levels whose depths are dependent on the water column depth. The minimum layer-thickness is about 50 cm nearshore (with a 15 m water column depth).

ROMS uses an Arakawa type C grid. The modeled domain extends from 47.5°N to 49.5°N in latitude and 6.5°W to 4.5°W in longitude (Fig. 1, B) at a horizontal resolution of 1.5 km. Topographic data were provided by the SHOM ('Service Hydrographique et Océanographique de la Marine').

2.1.2. Biogeochemical model

The physical model has been coupled to a biogeochemical, NPZD-type model (Fig. 2) which simulates some degree of phenotypic biodiversity among phytoplankton. Initially described in Follows et al. (2007), this 'Everything Is Everywhere' model allows the phytoplankton community to self-assemble according to environmental constraints (physical and biogeochemical properties) including biological interactions associated with interspecific competition and prey/predator relationships. The model simulates phytoplankton primary production based on local concentrations of phosphate, silicate, nitrate, nitrite and ammonium.

A large number (120) of phytoplankton phenotypes is initialized and evenly distributed between two size-classes, microphytoplankton (~10 μm Equivalent Spherical Diameter (ESD)) and picophytoplankton (~1 μm ESD). Each size-class is subsequently subdivided into two functional groups (Fig. 2). A microphytoplankton group includes diatoms (that require silicate for growth) and LND ('Large Non-Diatoms'); picoplankton are divided evenly between *Prochlorococcus*-like phytoplankton (PLP) which do not use nitrate and nitrites (Moore et al., 2002) and SNP ('small non *Prochlorococcus*') which use all three sources of inorganic nitrogen.

Each of the four functional groups is composed of 30 phenotypes, distinguished from each other by distinct growth parameters, affinity for nutrients and light and optimal temperature. Physiological parameters such as nutrient half saturation constants and light sensitivity are stochastically chosen for every phenotype depending on their functional group with theoretical allometric considerations. This method restricts values of phenotype parameters to lie within a defined range for each functional group (see Appendix A).

2.1.2.1. Growth rate and nutrients half saturation.
Unlike resource affinity and sensitivity to temperature and light, the maximum intrinsic growth rate is considered to be constant for all phenotypes of a given functional group but varies between functional groups (Follows et al., 2007). Thereby, large phytoplankton (*i.e.* diatoms and LND) exhibit a higher maximum growth rate but a lower affinity for nutrients ('r' strategy) (Furnas, 1990; Litchman et al., 2007) while smaller cells (SNP and PLP) are less competitive under nutrient saturating conditions but show a higher affinity for the substrate that make them more efficient under oligotrophic conditions ('K' strategy').

The increase in the maximum growth rate with increasing body size between functional groups is motivated by the fact that, below a size of ~5 μm ESD, an increase in cell size is shown to be linked to an increase in growth efficiency (Chen and Liu, 2010; Marañon et al., 2013). Noticeably, a negative correlation between cell size and growth rate is sometimes observed but rather concerns taxa within a single phylogenetic group such as the diatoms where some larger species possess a lower growth rate compared with smaller cells (Raven et al., 2005; Irwin et al., 2006).

Moreover, many studies (Chan, 1980; Furnas, 1990; Litchman et al., 2007) report that, for a same size, diatoms generally have a higher growth rate than other phytoplankton types. Therefore, within the
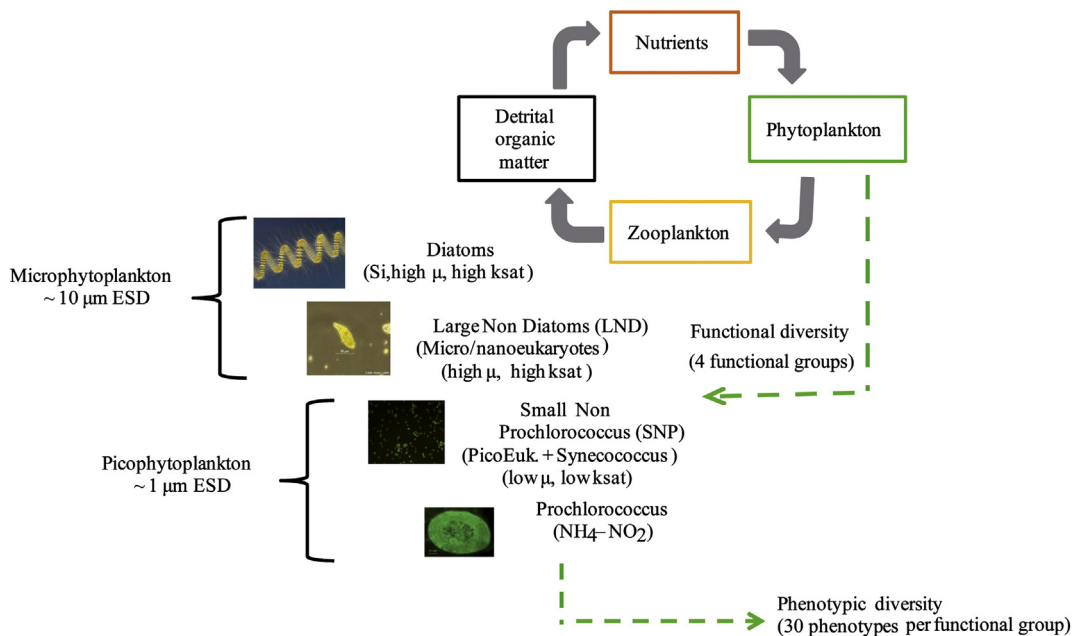

Fig. 2. Conceptual scheme of the biogeochemical model and its representation of phytoplanktonic diversity. (ESD) equivalent spherical diameter, (μ) maximum growth rate, (ksat) nutrient half-saturation constants.

large size class, modeled diatoms are assigned a higher maximum growth rate than LND.

Those maximum daily phytoplankton growth rates in this study are those used in Goebel et al. (2010) which focused also on a coastal region unlike the global study of Follows et al. (2007). Indeed, phytoplankton grows generally faster in coastal region than in pelagic ecosystems (Eppley and Thomas, 1969).

Half-saturation constants (κ) for nutrients for the two large phytoplankton groups have been parameterized specifically for this study. They have been modified from Follows et al. (2007) (0.56–0.88 mmolN·m^{-3}) toward higher values (*i.e.* 0.8–1.12 mmolN·m^{-3} for NO$_3$) in order to represent high κ observed for coastal species compared to offshore species. As an example, Eppley and Thomas (1969) measured nitrate half saturation constant for growth around 1.2–1.5 mmolN·m^{-3} for *A. japonica* diatoms while a more pelagic species (*C. gracilis*) has a κ of 0.2 mmolN·m^{-3}.

2.1.2.2. Light sensitivity. Large phytoplankton groups are given higher light requirements than smaller ones in our model. Consequently, small-size cells are generally able to grow under lower light levels than larger phototrophic cells (Glover et al., 1987; Edwards et al., 2015). This parameterization is based on a process, already stressed in the seminal work of Follows et al. (2007), related to the negative impact of the packaging effect of pigments on the efficiency of photosynthesis in large cells (Falkowski and Raven, 1997; Finkel, 2001). However, localization of diatoms in low light environments at the global scale has received attention lately (Brun et al., 2015), but it is yet unclear if their presence is related to low light requirements of some diatom species or the colocation of high nutrient concentrations in low light regions.

In the model, the growth rate sensitivity for light is governed by two parameters for each functional group according to the assumption discussed in the previous paragraph. First, k$_{par}$ defines the increase in growth rate with increasing light at low levels of irradiation. Conversely, k$_{inhib}$ corresponds to the decrease of photosynthesis due to photo-inhibition at very high light intensities. To account for the light response of temperate coastal phytoplankton, these parameters have been modified slightly from Follows et al. (2007). More precisely, the k$_{par}$ parameter for diatoms and LND have been adjusted using experimental values published by Maguer et al. (2011) to fit the optimum light required by large phytoplankton cells to perform photosynthesis in our study area (see table in Appendix A).

Owing to the lack of consensus on light inhibition that comes out to be more linked to environmental conditions of cells (acclimation) than size (Harrison and Platt, 1986; MacIntyre et al., 2002), the range of photoinhibition parameter (k$_{inhib}$) has been set to the same value in our four functional groups ($1.10^{-3} \pm 5.10^{-5}$ μEin·m^{-2}·s^{-1}). As a consequence, small-size cells with higher k$_{par}$ are further photo-inhibited for lower light irradiance compared to large cells.

2.1.2.3. Temperature sensitivity. Phytoplankton growth sensitivity to temperature also has no reason at present to be defined as a function of phytoplankton size. However, while *Synechococcus* sp. and small eukaryotes are ubiquitous and show a pole to pole presence (Legendre et al., 1999; Zubkov et al., 2000), *Prochlorococcus* sp. is encountered mainly in (sub)tropical, oligotrophic oceans where they dominate the photosynthetic biomass (Partensky et al., 1999). Indeed, no growth of *Prochlorococcus* sp. has been observed below 15 °C, and this genus is logically absent from the Iroise Sea observations. Reported optimal temperature for growth is usually around 22–24 °C (Suzuki et al., 2003; Johnson et al., 2006). The choice was made to keep this PLP group in our simulations to maintain 'everything is everywhere' model structure with four functional groups as close as possible to previous similar studies (Follows et al., 2007, Goebel et al., 2010). However, in order to take into account this physiological constraint on temperature optimum, no *Prochlorococcus* sp. analogs can be drawn with a temperature optimum under 20 °C.

Particulate detrital organic matter and microphytoplankton cells only are subject to sinking. Once sinking detrital organic matter reaches the bottom of the water column, only a small fraction (5%) is effectively buried. The remaining 95% is remineralized immediately within the deepest grid cell as inorganic nutrients. This process mimics the role of the benthic trophic chain in nutrient recycling within coastal systems (Le Pape et al., 1999).

Once a phytoplankton phenotype is considered extinct (below a fixed threshold (C$_{ext}$; table in Appendix A) everywhere in the model grid), it is randomly substituted by a new phenotype with a different adaptive strategy for growth but belonging to the same functional group. This new phenotype is homogeneously initialized across the whole area in a conservative way by removing material from inorganic nutrients to supply the corresponding phytoplankton compartment. In very rare cases where dissolved inorganic compartments are not sufficient, particulate organic matter or an abundant phytoplankton compartment (within the limit of 1% of the biomass) are used to enforce conservation.

The model also includes two zooplankton size classes: micro- and mesozooplankton whose diet preferences are established following prey/predator size ratios. Both feed on all phytoplankton preys and mesozooplankton also grazes on microzooplankton. Predator switching toward different available prey is set using a 'kill-the winner' (KTW) hypothesis, described in Vallina et al. (2014). The predator's preferences for the most accessible and profitable prey, is defined through the palatability parameter which depends on the predator-prey size-ratio. Picoplankton is thus more palatable for microzooplankton whereas mesozooplankton grazes preferentially on microphytoplankton. Diatoms are considered as less palatable to mesozooplankton than LND due to their shape and siliceous frustule. Detailed values of all parameters used for representing zooplankton's food preferences are given in Appendix A. Unlike palatability, assimilation efficiencies are made equal for all prey: a proportion of 30% of the total ingested food is effectively assimilated for both microzooplankton and mesozooplankton. This assimilation efficiency have no reason to vary with cell size or between taxa (ciliates and copepods) (Straile, 1997).

The maximum grazing rate (grazemax) of microzooplankton is higher than the mesozooplankton's one (Hansen et al., 1997). Conversely, the grazing half-saturation constant (ksatgraz) has been shown to be independent of body size (Hansen et al., 1997) and thus does not vary across our two zooplankton size-classes (0.07 mmolP·m^{-3}).

Natural mortality representing various processes (*e.g.*, cell lysis and parasitism) is parameterized as linear with biomass for all phytoplankton and zooplankton. A classical quadratic mortality is added for mesozooplankton in order to account for density-dependent predation by higher trophic level predators. Indeed, the combination of a linear closure term with a quadratic one has been shown to reduce the occurrence of oscillatory behaviors in ecosystem models (Edwards and Yool, 2000).

Organic matter resulting from mortality, excretion and sloppy-feeding is transferred to sinking particulate organic matter and dissolved organic matter pools which are then remineralized into nutrients by implicit heterotrophic bacterial activity. The remineralisation rate of dissolved organic matter of 0.2 day^{-1} (see Appendix A) has been increased by tenfold compared to the original value of 0.02 day^{-1} (Follows et al., 2007) in order to maintain reasonable levels of inorganic nutrients available for phytoplankton growth compared to *in-situ* data. Indeed, this original value resulted in an excessively long turnover time of organic matter within the detrital dissolved pool.

Phytoplankton and zooplankton biomass are expressed in phosphorus concentrations and a constant Redfield Ratio is used to convert phosphorus-based biomass to nitrogen and carbon contents. Phytoplankton chlorophyll concentration is not explicitly simulated but calculated *a posteriori* using constant C:Chl for each functional group for comparison with observed biomass estimates. Small phytoplankton is assumed to have higher C:Chl of 300 gC·gChl^{-1} compared to LND

(100 gC·gChl^{-1}) and diatoms (50 gC·gChl^{-1}) as detailed in Goebel et al. (2010).

For a more complete description of equations and trade-offs that are implemented in the model, see Follows et al. (2007) and Dutkiewicz et al. (2009). The biogeochemical equations are the same as the ones presented in the Supporting Online Material of Follows et al. (2007) except for the grazing 'KTW' formulation that is similar to Vallina et al. (2014). A complete description of parameters that have been used in the present study is presented in Appendix A.

2.2. Initial and boundary conditions

The surface atmospheric forcing conditions (wind stress and heat fluxes) are provided by the ALADIN atmospheric model from the French National Center for Meteorological Research (CNRM) with a spatial resolution of 0.1° and a temporal frequency of 3 h. These fields were interpolated over the model grid with a rectangular bivariate spline function. Both short- and long-wave solar radiation are derived from the Spinning Enhanced Visible and Infrared Imager (SEVIRI) which provides 3 km resolution images every 15 min. These fields are used by the hydrodynamic ROMS model following the COAMPS (Coupled Ocean/Atmosphere Mesoscale Prediction System) bulk formulation from Liu et al. (1979). A solar diurnal cycle is applied with day/night periods and the phytoplankton growth rates are thus adjusted accordingly.

Tidal forcing was added using the regional NEA (North-East Atlantic) tidal atlas T-UGOm 2D ('Toulouse Unstructured Grid Ocean model'), obtained from the POC, 'Pôle d'Océanographie Côtière de Toulouse') which represents sea surface elevation (amplitude) and barotropic tidal currents for 15 harmonics. The quarter-diurnal tidal compound M4, which is known to be of primary importance to properly simulate the tidal signal in the Bay of Biscay (Pairaud et al., 2008a, 2008b), is included.

Consistent initial and lateral open boundary conditions were obtained from a NEMO-PISCES North-Atlantic basin simulation having a horizontal resolution of 1/4° and temporal average saved every 5 days for both physical (temperature, salinity and flow velocities) and biogeochemical fields (NO$_3$, PO$_4$ and SiO$_2$). Preliminary comparisons between NEMO-PISCES nutrient fields and a large set of historical *in-situ* data (Sourisseau, pers. comm.) have shown an underestimation of both nitrate and phosphate levels but an overestimation of silicate levels. On the basis of these observations, corrections to initial and boundary conditions from the NEMO-PISCES simulation have been implemented using constant conversion factors in time. Phytoplankton phenotypes, not simulated in the large scale simulation used for boundary conditions, are treated by a zero gradient conditions at the open boundaries.

Two rivers (Aulne and Elorn) are included in our configuration. Flow rates and water temperature were collected by the 'Agence de l'eau Loire-Bretagne' (http://osur.eau-loire-bretagne.fr) and nutrients (NO$_3$, PO$_4$ and SiO$_2$) were supplied weekly by ECOFLUX observatory between 1998 and 2012 (http://www-iuem.univ-brest.fr/ecoflux). A monthly climatology of these data was used in our simulations.

2.3. Numerical implementation and experimental design

For sake of consistency between tide ranges and atmospheric and lateral forcing, we used a set of realistic forcing conditions (year 2007) rather than climatological data. Nonetheless, our goal was to reproduce a classical seasonal cycle in the Iroise Sea without claiming to simulate a particular year. This single set of forcing was repeated three times. The single repetition is used as a spin-up. Simulating two repetitions of an identical year of forcing is sufficient for our purpose as initial conditions are lost quickly within few weeks. Indeed, we found that the second and third years were consistent in both physical and biological modeled fields. Only the third year was however retained for analysis. An ensemble of five simulations was run to account for the impact of the random initial choices for biological growth parameters.

2.4. Cluster analysis

To distinguish meaningful biogeographical provinces based on physical features within the water column, a *k-means* clustering algorithm (Jain et al., 1999) was used. This partitioning method assigns data points to a pre-defined number of domains by minimizing the squared Euclidean distance between the data points within a cluster and maximizing the distance between the different clusters. Centers are initially assigned randomly among data values and are then recalculated repeatedly until convergence is achieved (Gan et al., 2007). To avoid any influence of the initial choice of centers, 10 iterations of the process are repeated and the minimum sum of distances is selected. Based on our knowledge of Iroise Sea dynamics, and as is usually done for studying tidal fronts (Videau, 1987; Sournia et al., 1990), the number of domains was fixed to three sub-regions. Lateral boundary layers and shallow bays of Brest and Douarnenez (see Fig. 1B), for which the model resolution is inadequate to provide good representation of open sea exchanges, were omitted from the clustering.

As the purpose of this study is to identify existing links between physical processes and biogeochemical properties, we based our clustering method on the main physical characteristics that relate to the vertical stability of the water column. This set-up leads to the identification of relevant hydrodynamical sub-regions that contrast in terms of dynamical attributes and enables us to test if these regions are also distinguished from each other for biogeochemical and ecological properties.

Variables selected to perform the *k-means* analysis are (i) the time averaged temperature difference between the bottom and surface (°C) and (ii) the maximum vertical temperature gradient (°C·m^{-1}). Due to the spatial movement of the frontal position over time and to avoid rough longitude/latitude segmentation, this clustering method was applied to monthly averaged model output. We found that the distinction between three different sub-regions by our criteria was possible between May and October.

Several tests were conducted to optimize the definition of the sub-regions. Increasing the number of domains decreases the clustering confidence assessed by the silhouettes method, which is a measure of similarity between each point of its own cluster compared to points in other clusters (Kaufman and Rousseeuw, 1990). This value ranges from 1, indicating that a given point is very distant from neighboring clusters to −1, which indicates that the point is assigned to the wrong cluster. In our case, the average silhouette value of our data points is a relatively good value of 0.83 (averaged over the whole period of the Ushant Front's presence) if three clusters are chosen.

2.5. Fitness evaluation

To understand the distribution of the different modeled phytoplankton phenotypes, their relative competitive abilities have been evaluated following the resource competition theory (Tilman, 1987). The equilibrium resource concentration of a nutrient is denoted as R* and represents the nutrient concentration at which, for a given phytoplankton phenotype, total gains balance total losses (*i.e.*, the net growth is equal to zero). This concentration at equilibrium can be computed for each phenotype and is determined by its characteristics including maximum growth rate (μ_{max}), half saturation constant (κ) and the rate of loss processes, such as natural and grazing mortality (m). For example, for phytoplankton *j*, R$_j^*$ for phosphorus is computed as follows:

$$R_j^* = \kappa_{PO_4} * m / (\mu_{max} - m)$$

Competitive exclusion theory implies that, at equilibrium and in stable environmental conditions, the species with the lowest R* (R$^*_{min}$) will be the most competitive (*i.e.* have the highest fitness) and other organisms will be excluded over time. This competitive exclusion occurs as long as many species are competing for a single resource. Under

stationary conditions, the concentration of this resource would then be drawn down to the R^*_{min} concentration. However, the complex and dynamic behavior of environmental conditions in the ocean and the existence of many limiting resources lead to coexistence between many species into phytoplankton assemblages (Hutchinson, 1961; Chesson, 2000; Klausmeier et al., 2007).

2.6. Observational data

To quantitatively evaluate model performance, output has been compared to climatological (2003–2014) temperature estimates (Sea Surface Temperature, SST) from Moderate Resolution Imaging Spectroradiometer (MODIS) (http://oceancolor.gsfc.nasa.gov/cgi). Surface chlorophyll estimates were also obtained from MODIS ocean color sensors data converted to chlorophyll concentrations for the 2003–2007 period following the modified OC4 algorithm proposed by Gohin et al. (2002). This algorithm has been shown to be very efficient for coastal waters for which optical properties are periodically dominated by suspended matter. This product was available with a spatial resolution of 0.015°, which is very close to our grid resolution. Model output has been interpolated over the MODIS data grid to perform these comparisons.

In addition to satellite validation, model performance simulating temperature, total chlorophyll and nutrient profiles have been assessed using a large set of *in-situ* data distributed over the whole study area (using a Seabird SBE49 CTD, Seapoint FLNTU fluorometer and nutrients obtained from a ran and Luebbe AutoAnalyser II). These data have been compiled from two different cruises (FroMVar 2007 and 2009) which took place along a transect covering all hydrographic features encountered in the Iroise sea ecosystem (48°08′ N).

Finally, the phytoplankton community structure in terms of the functional groups and size was also compared to *in-situ* measurements in the coastal mixed area (data provided by 'Service d'Observation en Milieu Littoral, INSU-CNRS, Brest'). These data are sampled at high tide, at the entrance of the bay of Brest (Ste-Anne-du-Portzic: 48°21′ N; 4°33′ W; 10 m depth). They are representative of water masses from outside the Bay of Brest, highly mixed by tidal currents and exchanged with the open ocean during a tidal cycle. These *in-situ* samples have been analyzed by microscopy and flow cytometry that allows discrimination and enumeration of specific subgroups based on their size and fluorescence characteristics as described in Marie et al. (1999). This latter method provides us the abundance of the smallest size

class (three classes of picoplankton: *Synechococcus* sp., *Prochlorococcus* sp., picoeukaryotes and nanoeukaryotes) while the abundance of larger groups comes from microscopic counts. Conversion from cell abundance to carbon biomass has been performed using relationship factors from Verity et al. (1992). Results presented are weekly averages from 2009 to 2012 measurements for small cells and from 1998 to 2012 for larger ones.

3. Results

3.1. Model validation

3.1.1. Temperature distribution

The Taylor diagram (Fig. 3 A) displays good agreement between model results and MODIS data for the monthly average SST distribution for well-mixed, stratified and frontal regions. The global correlation coefficient is 0.91 (*i.e.* whole domain labeled as 'global' in Fig. 3A). A slightly lower correlation coefficient of 0.89 is found for the mixed waters mainly corresponding to the coastal and North East areas, which are vertical homogenized by tidal currents throughout the year. This lower correlation coefficient reflects an overestimation of the temperature in the well-mixed coastal area and along the North coast by the model during summer compared to satellite data (see also Fig. 4A and B). Consequently, the standard deviation is lower in the model than in satellite data for this well-mixed region (Fig. 3A).

The main feature of interest in the Iroise Sea ecosystem, the Ushant Front, is present essentially during the summer season, with maximal intensity reached in August–September; there is a greater interest in evaluating model performance during this period than for the rest of the year. Comparison of August–September MODIS and modeled SST (Fig. 4A and B) over the entire domain reveals similar patterns. The highest surface temperature of ~18 °C is found offshore, in the stratified waters to the west of the tidal front (which is located approximately along the 100 m isobath; Fig. 1B). Along the coast, surface temperature also exhibits high values inside shallow bays of Brest and Douarnenez with a temperature decrease westward. However, over continental shelf waters which are strongly mixed by the intense tidal currents east of the Ushant front, SST does not exceed 15 °C. Model outputs show slightly lower amplitude of the zonal temperature gradient than satellite-derived data. The three clusters presented in Fig. 4 (A and B) are computed using two-month average (August–September) of physical properties and identify three different hydrodynamical regimes in
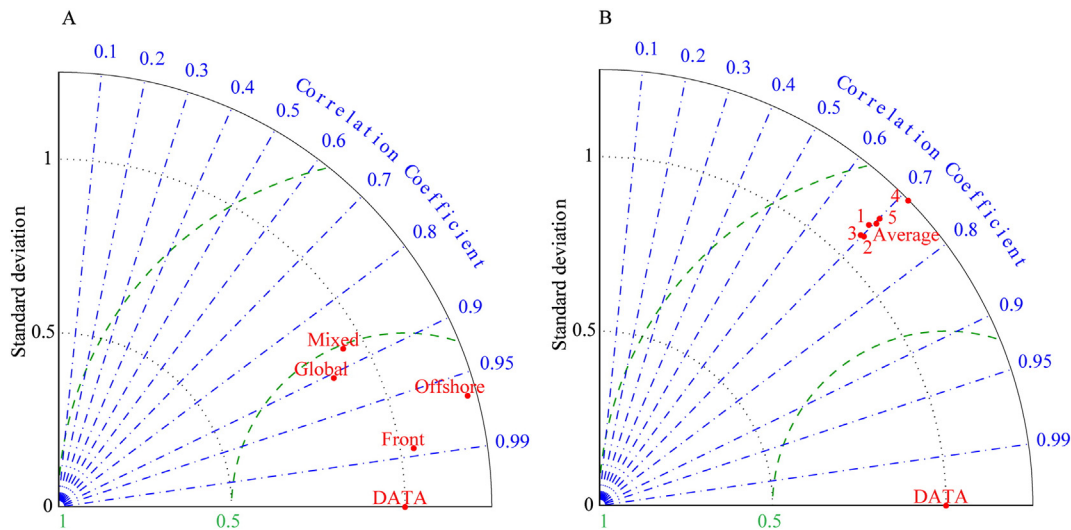

Fig. 3. Taylor diagrams for: (A) monthly averages of model outputs and MODIS observations of Sea Surface Temperature (°C) for the entire domain (labeled as 'Global' in the figure) and for the three sub-regions defined by k-means clustering analysis (Offshore, Front and Cosatal-Mixed areas) and (B) year-averaged chlorophyll concentrations (mg·m⁻³) for modeled surface level and MODIS - derived data computed from the entire domain, for each of the five repetitions of the simulation and for the average simulation designed from these five repetitions (labeled as 'Average').
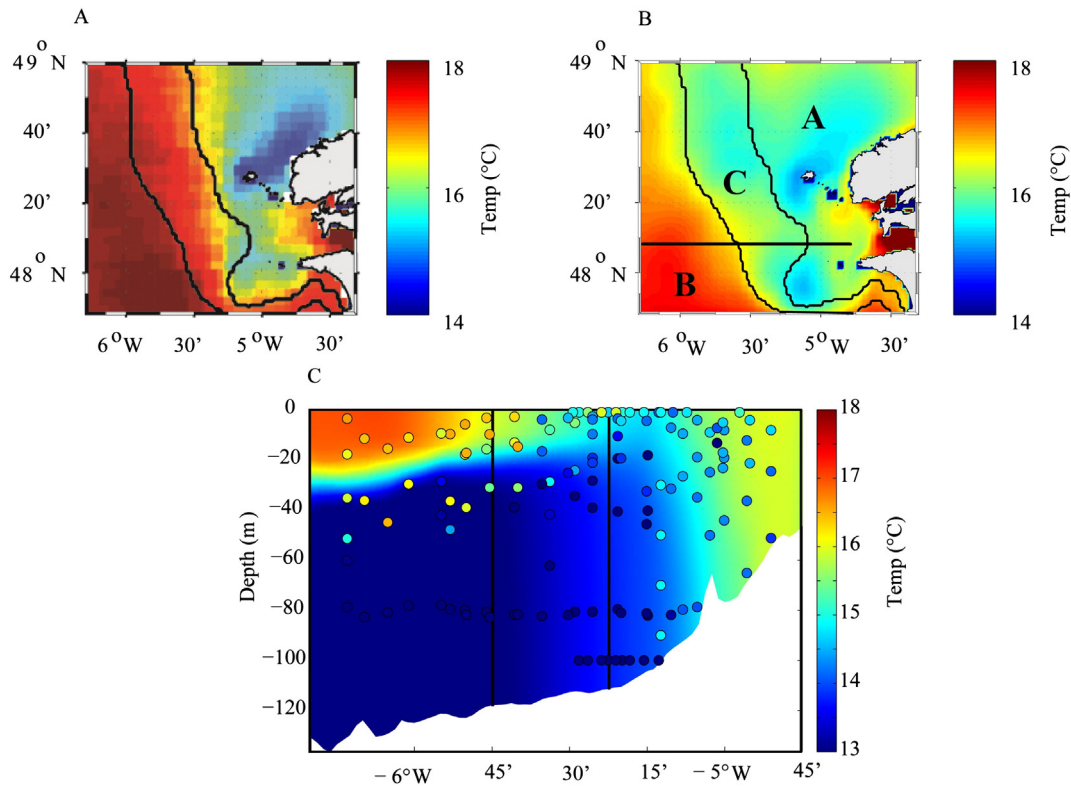
Fig. 4. Sea Surface Temperature from (A) satellite MODIS climatological data and (B) model output during the summer (August–September average). (C) Vertical distribution of modeled temperature along the 48°08′ N transect (black line in B) in September (monthly average) with *in-situ* data sampled during the FroMVar cruises (September 13 to September 15, 2007 and 19 to 29 September 2009). The contours of the three sub-regions coming from the *k-means* clustering analysis (computed from August–September averages of physical fields) are drawn on each panel (black lines). A: well-mixed coastal waters; B: offshore stratified waters and C: frontal area.

terms of vertical mixing and stratification. (i) The mixed area (region A) comprises nearshore waters which exhibit weak seasonality in the deep mixed layer depth, with strong vertical mixing exerted by tidal friction along the continental shelf occurring throughout the year and preventing seasonal stratification from forming: this mixed region concerns also the North East part of the modeled domain with depths < 90 m and shallow waters around the islands. (ii) The stratified area (region B) corresponds to the offshore part of the Iroise Sea that is conversely characterized, during the summer, by a substantial vertical temperature gradient between surface warm waters (~17 °C) and deep, colder waters (~13 °C). (iii) The frontal area (region C) separates the two latter regions (A and B) and constitutes a transitional zone where isopycnals rise to the surface.

From sea surface temperature maps (Fig. 4A and B), the modeled maximum zonal temperature gradient at the surface is located in the vicinity of the front predicted by *k-means* analysis. However, this modeled maximum horizontal SST gradient (*i.e.* frontal area) occurs to the west of that identified in satellite-based climatological data, indicating a zonal shift in the front position between model output and satellite-derived data.

The vertical modeled temperature structure in September (monthly average) along the 48°08′ N transect (Fig. 4C) is consistent with *in-situ* data sampled during two FroMVar cruises carried out in the Ushant Front area in September 2007 (Le Boyer et al., 2009) and September 2009 (Schultes et al., 2013 and Landeira et al., 2014). The maximum temperature found above the thermocline in region B is close to observations (~17 °C). The vertical temperature structure simulated by the model exhibits a shift between the position of the surface front (~ 5°30′ W) and the eastward position of the bottom front (~5°10′ W) (Fig. 4C). Unlike satellite date (Fig. 4A), the surface front zonal position in *in-situ* data at 48°08′ N, fits with modeled surface front position, within expected limits from the clustering analysis (Fig. 4C).

Modeled temperature in well-mixed waters (15.5–16 °C) is slightly overestimated compared to observed values (<14.5 °C), leading to a weaker zonal gradient in the model than in data between the mixed and stratified regions at the surface and a conversely steeper modeled zonal gradient at depths exceeding 30 m. Consequently, the position of the bottom is less apparent in FroMVar data than in model output (Fig. 4C).

Furthermore, the thermocline in the seasonally stratified part of the Iroise Sea (~6°12′ W) is deeper in cruise data (~45–50 m) than in model output (~30–35 m). For both model and *in-situ* data, the thermocline becomes shallower as one moves eastward, from the offshore stratified portion of the Iroise Sea to the surface front position (~5°30′ W) where it reaches the surface (Le Boyer et al., 2009).

3.1.2. Biogeochemical robustness among simulations

Simulated phytoplankton community has emergent characteristics in terms of biogeography and diversity that could be related partly to randomly assigned specific traits at initialization. To ensure the robustness of our results, we tested five realizations of the simulation using different initialization of phenotypes (see Section 2.3) and assessed the similarities of their results.

For this purpose, annual mean, spatially distributed surface chlorophyll distributions for the five simulations were compared to the most extensive data set provided by satellite (Gohin et al., 2002) (Fig. 3B). All simulations have similar correlation coefficients (~0.7) although their standard deviations exhibit some scatter. The ensemble average normalized standard deviation is 1.136 times the standard deviation found in the MODIS estimated chlorophyll data. Thus, all runs lead to similar results in terms of their annually averaged total chlorophyll distribution despite their differences in initially assigned phenotypes. Therefore, subsequently presented results are based on the ensemble average between each of the five realizations of the simulation.

3.1.3. Chlorophyll distribution

During summer (August–September average) (Fig. 5A and B), the highest surface biomass is clearly found at the Ushant front in both model output and the satellite-derived dataset but the largest chlorophyll concentrations are greater in model output (>1.5 mg·m^{-3}) than in the data (~1.2 mg·m^{-3}). For both satellite fields and model output, the north-east part of the domain reveals an intermediate level of total chlorophyll concentration (~0.8 to 1 mg·m^{-3}) whereas offshore oligotrophic surface waters exhibit very low chlorophyll levels.

The vertical chlorophyll structure along the 48°08′ N transect during September (monthly average) is shown in Fig. 5C. Modeled chlorophyll levels exceeding 2 mgChl·m^{-3} are encountered at the surface near the position of the front. Values of the same order of magnitude were measured during the FroMVar cruises. Conversely, the mixed water column east of the front has modestly higher levels of chlorophyll in the model output (~1 mgChl·m^{-3} for depths between 50 and 80 m at ~5°10′ W) compared to *in-situ* data (<0.8 mgChl·m^{-3}). In offshore, stratified waters, the surface mixed layer depth is shallower in the model than in
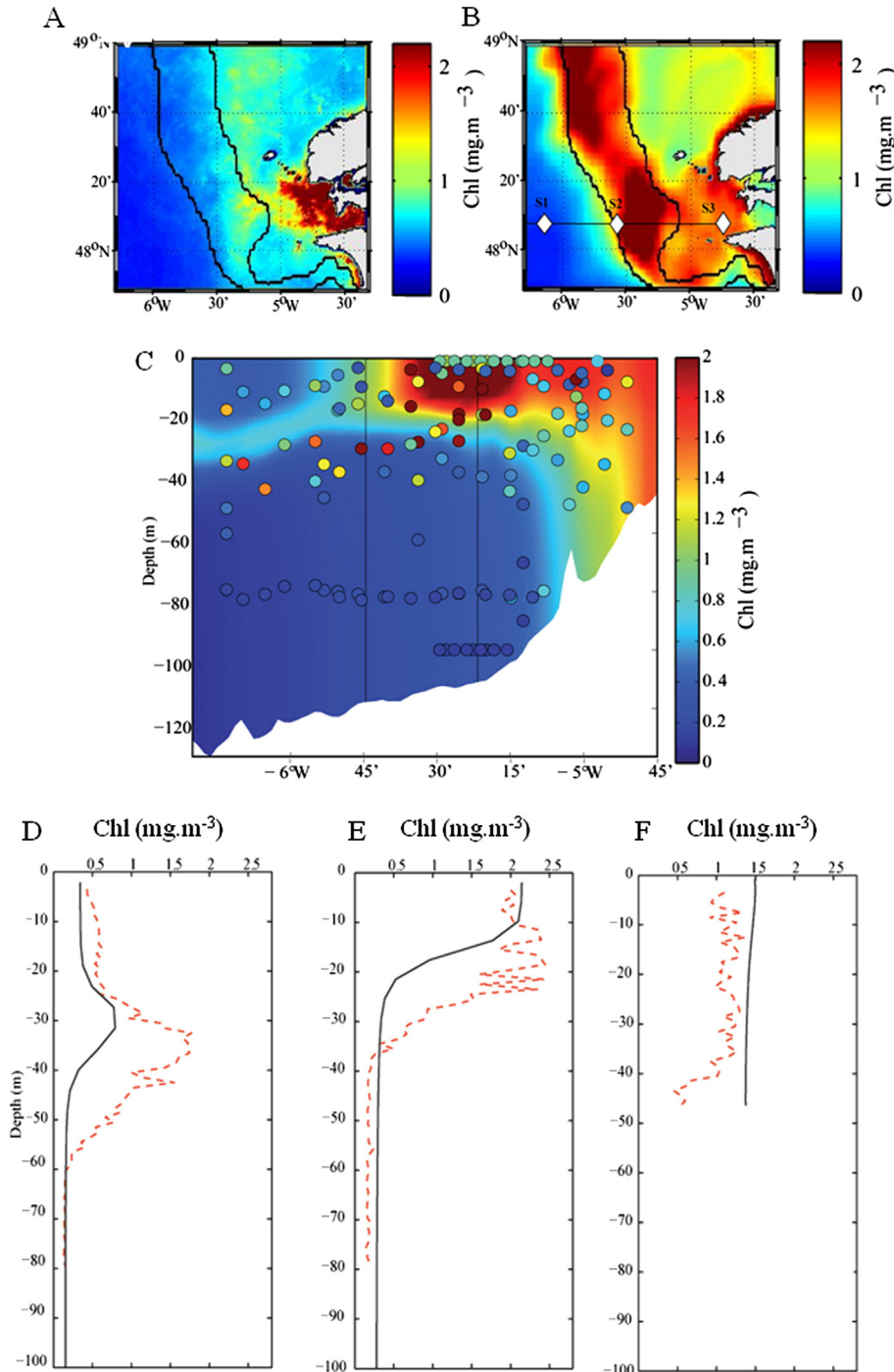

Fig. 5. Surface chlorophyll concentrations from (A) satellite MODIS climatological data and (B) model output during the summer (August–September average). (C) Vertical distribution of modeled chlorophyll along the 48°08′ N transect (black line in B) in September (monthly average) with *in-situ* data sampled during the FroMVar cruises (September 13 to September 15, 2007 and 19 to 29 September 2009). Chlorophyll concentrations vertical profiles at (D) station 1: 48°08′ N; −6°10′ W; 19 September 2009, (E) station 2: 48°08′ N; −5°35′ W; 28 September 2009 and (F) station 3: 48°08′ N; −4°45′ W; 29 September 2007 of the 48°08′ N transect for both *in-situ* data (dotted red line) and model output (black solid line) (see panel B for station locations). The contours of the three sub-regions coming from the *k-means* clustering analysis (computed from August–September averages of physical fields) are drawn on each panel (black lines). (For interpretation of the references to color in this figure legend, the reader is referred to the web version of this article.)

data and chlorophyll levels are underestimated (0.8 mgChl·m^{-3} in the Deep Chlorophyll Maximum (DCM) for the model compared to >1.5 mgChl·m^{-3} within DCM during the FroMVar cruises; see also Fig. 5D).

Three stations selected from the 48°08′ transect (Fig. 5D to F) exhibit very different vertical profiles of total chlorophyll, and this vertical structure is quite similar between model output and *in-situ* data. The eastern station (Fig. 5F: 48°08′ N; 4°45′ W) reveals a homogeneous, well-mixed water column with chlorophyll concentrations of about 1.2 mg·m^{-3}. Conversely, the western profile (Fig. 5D: 48°08′ N; − 6°10′ W), located in the offshore stratified area exhibits a clear DCM at ~35 m. At the Ushant front position (Fig. 5E: 48°08′ N; −5°35′ W), the surface waters show the highest levels of chlorophyll with concentrations around 2 to 2.5 mgChl·m^{-3} and marked variability between 15 and 25 m depth in field measurements. This high-chlorophyll surface layer is approximately 20 m thicker in the data (~35 m) than in the model output (~15 m).

Below 40 m depth, chlorophyll concentrations decrease with depth to <0.5 mgChl·m^{-3} in the light-limited, deep layer (Fig. 5E).

3.1.4. Nutrient distributions

The overall vertical structure of nutrients in our simulations (Fig. 6) is in agreement with *in-situ* data showing a general depletion of the three major nutrients (NO_3, PO_4 and SiO_2) in the surface layer of the open ocean (west of the front; region B) during the summer. In the deep layer of these stratified waters (whose upper limit is deeper in observations compared to model output), nutrient concentrations are high as phytoplankton growth is light limited and chlorophyll levels are low (Fig. 5C and D). In the coastal well-mixed region (region A and to a lesser extent in the region B and C), nitrate concentrations (~5 mmol·m^{-3}) are slightly overestimated by the model (Fig. 6A) when compared to *in-situ* data (3 to 4 mmol·m^{-3}) while silicate (Fig. 6C: ~1.5 mmol·m^{-3}) and phosphate concentrations (Fig. 6 B: ~0.2 mmol·m^{-3}) are slightly underestimated.

3.1.5. Primary production

In the August–September average, vertically integrated chlorophyll-based biomass from our model (Fig. 7A) is largest in the eastern part of the frontal area and in the north-east part of the domain (70–80 mgChl·m^{-2}). Similarly, maximum values of daily primary production (Fig. 7B) occur near the front and in the well-mixed waters of region A, over the continental shelf. Highest values are found along the north coast where it reaches >1500 mgC·m^{-2}·day^{-1}.

However, this similarity between the vertically integrated chlorophyll and primary production patterns does hide differences in their vertical structure (see Figs. 5C and 7C; the 48°08′ N transect). Indeed, the vertical structure of chlorophyll shows a homogeneous distribution over the whole water column in the well-mixed area (Fig. 5C) whereas in the same area the primary production is restricted to the 0–20 m upper layers (Fig. 7C). Consequently, the surface primary production displays the same overall spatial distribution than its vertically integrated counterparts (with negative east-to-west gradient and maximum values in the well-mixed eastern area, Fig. 7B and C), while the surface chlorophyll maximum is restricted to the Ushant Front position (unlike its vertically integrated counterpart, Fig. 5B *vs.* Fig. 7A).

For both biomass and primary production, lowest values are simulated in surface waters of the oligotrophic, offshore area (region B).

3.1.6. Assimilation number

The vertically averaged assimilation number (*i.e.* photosynthetic rate per unit amount of chlorophyll) decreases from the open sea to the Ushant Front (region C), where it reaches its lowest values (0.4 mgC·mgChl^{-1}·h^{-1}; Fig. 8A) associated to low vertically average photosynthetic available light of ~100 W·m^{-2} over the 0–20 m upper layer (Fig. 8B). Indeed, despite very high phytoplankton biomass (Fig. 5), the modeled carbon fixation at the surface of the Ushant front does not exceed 1 mgC·mgChl^{-1}·h^{-1} (Fig. 8C). Modeled maximum
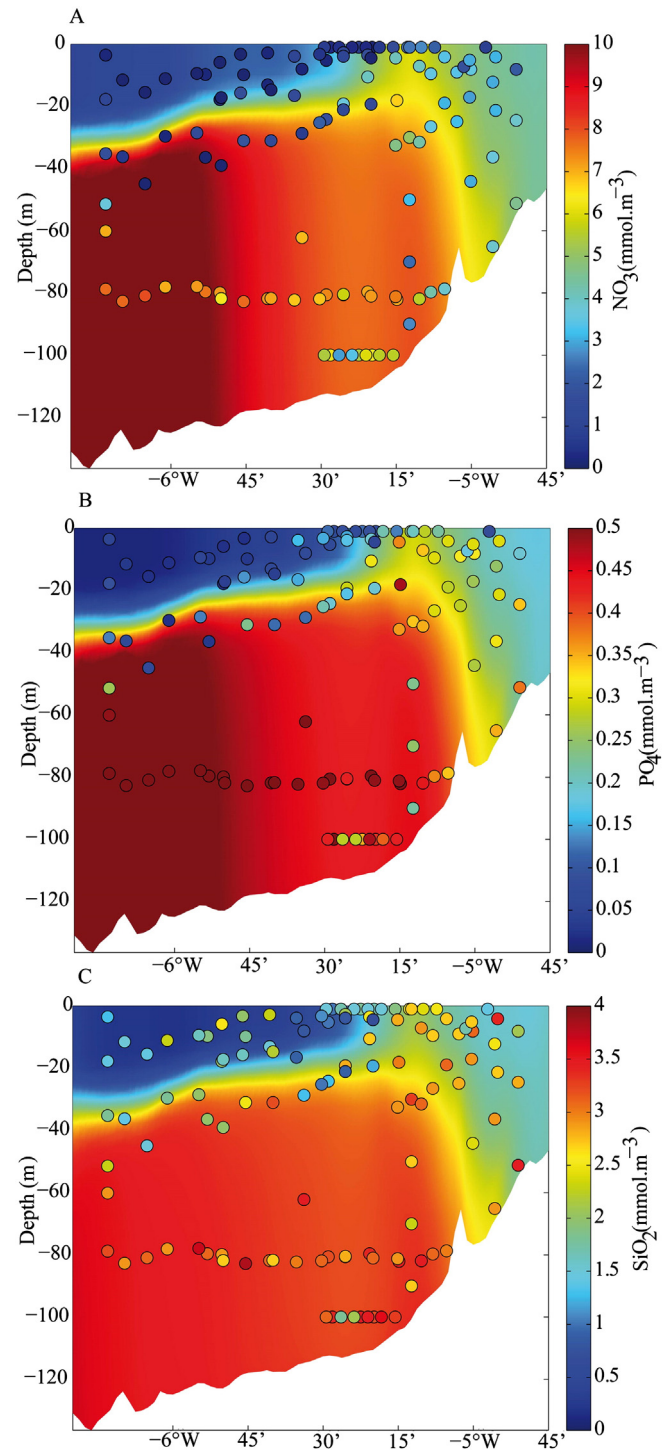

Fig. 6. *In-situ* concentrations of main macronutrients (A) nitrates; (B) phosphate and (C) silicates (scattered circles) sampled during the FroMVar cruises (September 13 to September 15, 2007 and 19 to 29 September 2009) superimposed to simulated summer concentrations (August–September average) along the 48°08′ N transect (see Fig. 1).

vertically averaged values of ~1.2 mgC·mgChl^{-1}·h^{-1} are found in shallow near-shore waters and around the islands (Fig. 8A).

Indeed, along the 48°08′ N transect (Fig. 8C), high assimilation numbers (>2 mgC·mgChl^{-1}·h^{-1}) are found in the surface layer of the well-mixed waters nearshore (region A), correlated with maximal primary production values (Fig. 7C). Finally, the DCM in the stratified west waters offshore (region B) shows intermediate assimilation number values of ~1.2 mgC·mgChl^{-1}·h^{-1}.
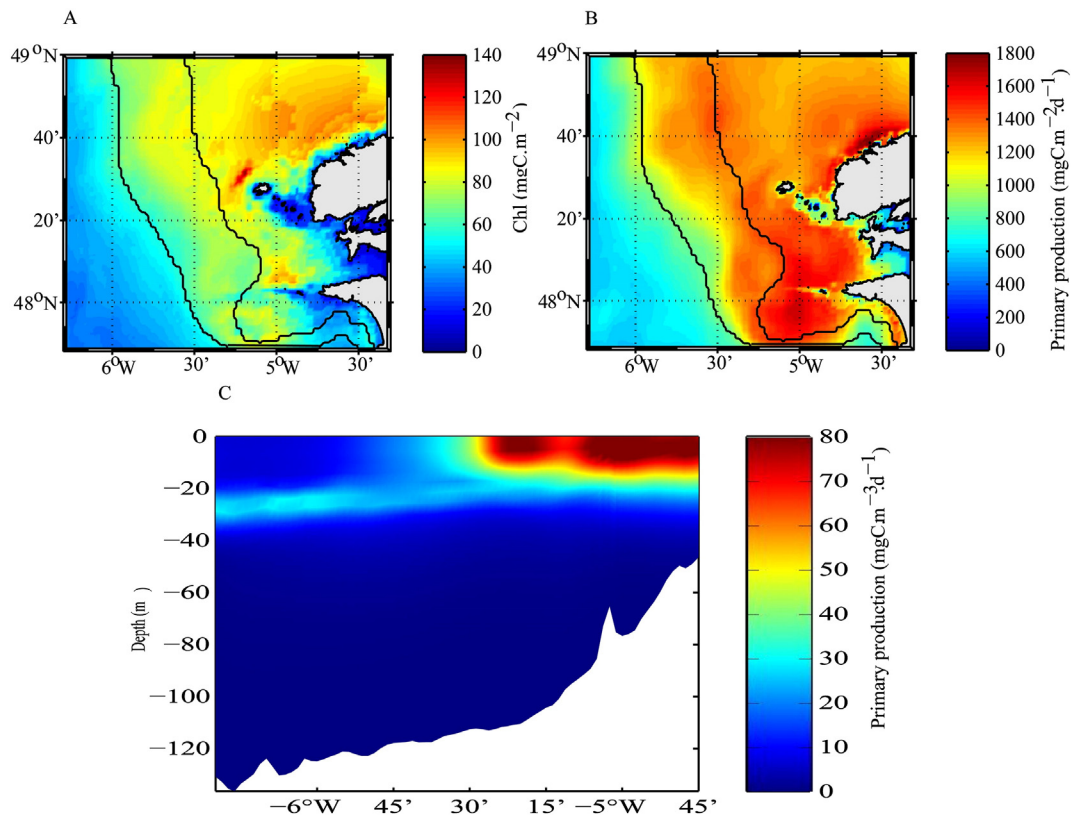
Fig. 7. Vertically integrated (A) chlorophyll concentrations and (B) primary production during the summer (August–September average). C: Vertical distribution of modeled primary production along the 48°08′N transect (see Fig. 1) in September. Black contours on panels A and B are the limits of the three clusters coming from the *k-means* analysis (August–September average).
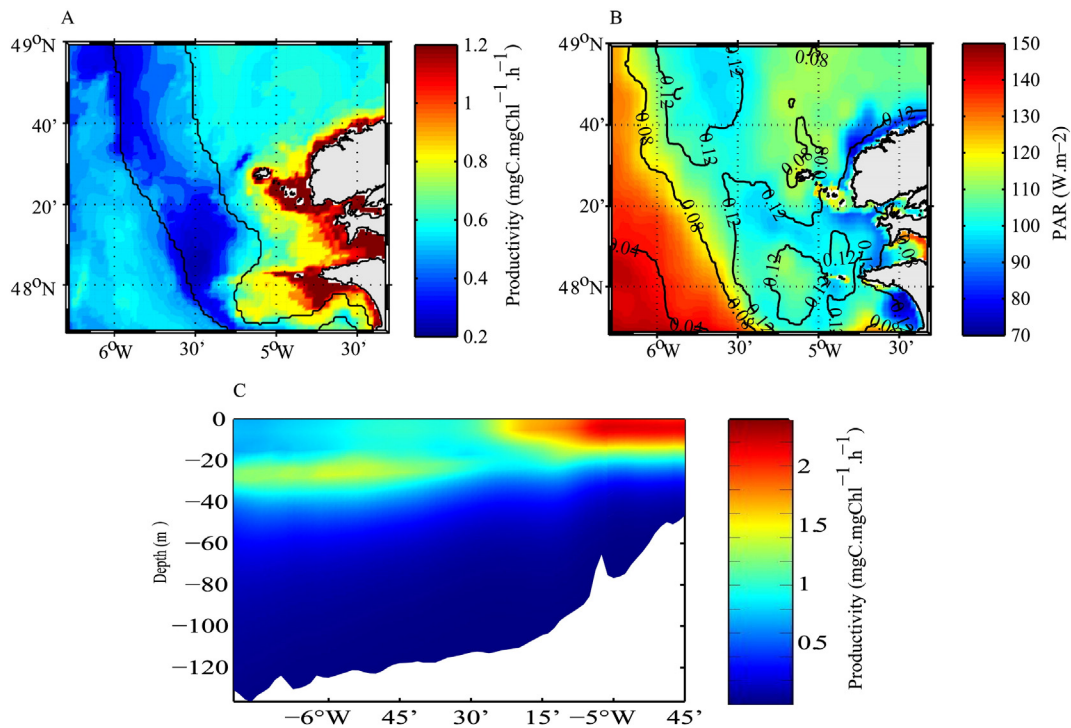

Fig. 8. (A) Vertically averaged assimilation number during the summer with limits of the three clusters coming from the *k-means* analysis (August–September average). (B) 0–20 m average Photosynthetic Available Radiation (contours are total phytoplankton biomass (gC·m^{-2}). (C) Vertical distribution of assimilation number along the 48°08′ N transect (see Fig. 1) in September.

3.2. Seasonal patterns and bioregionalization of total chlorophyll

As shown in the Hovmöller diagram at 48°08′ N (Fig. 9), the modeled phytoplankton bloom is initiated at the end of winter (February) within the coastal strip (Fig. 9B). It occurs later (April–May) but with greater intensity in the surface of the western/offshore part of the domain for both model output and satellite data. This process occurs as days-length gradually extends and stratification is developing, leading to better light availability for photosynthesis which was light-limited during the winter in deep waters. In April and May, the presence of nutrients combined with sufficient light irradiance in the surface layer of the offshore stratified water column enables photosynthesis to occur. Chlorophyll concentrations reach levels of 2.5 mg·m^{-3}. The surface layer becomes then oligotrophic relatively quickly and simulated chlorophyll levels fall close to zero in June. This collapse occurs earlier in satellite data (beginning of May) than in model output (Fig. 9).

From June to August, phototrophic biomass is mainly confined to the coastal area, supported by relatively high levels of nutrients (Fig. 6) supplied by local remineralisation in the whole tidally mixed water column. Modeled summer concentrations are around 1–1.5 mg Chla·m^{-3}, slightly higher than satellite estimates, as previously noted. Near the end of the summer period (late August), the modeled frontal position shifts westward while winds promote increased mixing over the continental slope. In September–October, high levels of total chlorophyll (comparable to those of spring bloom) are simulated within the Ushant front, which is located to the west of its satellite-derived counterpart.

The seasonal cycle of chlorophyll concentrations within our three regions obtained by *k-means* clustering is displayed in Fig. 10. During winter months (November to April), it is not consistent to define more than one sub-region based on our consideration of physical characteristics of the water column (see Section 2.4). Indeed, intense wintertime vertical mixing prevents stratification over the whole modeled area. According to our criteria of temperature vertical structure, only one cluster is

thus defined during these months while three clusters, corresponding to (i) well-mixed waters, (ii) well-stratified waters and (iii) frontal area, derive from the k-means clustering method from May to October. Therefore, the well-mixed area corresponds to the whole domain during winter and to the coastal/north east part of the Iroise Sea during spring to autumn.

The coastal and north east regions are vertically homogeneous system all along the year including during the summer (from March to October) with a total chlorophyll concentration remaining rather constant (~1 mg Chla·m^{-3}) during this period (Fig. 10A).

Conversely, the offshore system exhibits two characteristic peaks of chlorophyll (Fig. 10B) typical of temperate seas: a major peak, in May, with levels of chlorophyll higher than 2 mg Chla·m^{-3} and a minor autumnal peak in late August–September (~1 mg Chla·m^{-3}). Between those two peaks, autotrophic biomass is very low, surface primary production is then strongly controlled by low nutrient concentrations. Finally, the Ushant Front constitutes an intermediate total phytoplankton dynamic (Fig. 10C), with relatively high summer concentrations particularly in September. Unlike the offshore region, the highest peak of the frontal zone (~2 mg Chla·m^{-3}) takes place in autumn.

3.3. Phytoplankton community composition and distribution

3.3.1. Surface distribution

Total phytoplankton is divided into four functional groups (diatoms, large Non Diatoms (LND), Small Non *Prochlorococcus* (SNP) and *Prochlorococcus* sp. analogs (PLP)). Each functional group exhibits different temporal variations and surface zonal distributions (Figs. 11 and 12).

3.3.1.1. Well-mixed area. In the unique region defined as the whole Iroise Sea during winter by our clustering method, small cells (SNP) are responsible for the major part of the total phytoplankton biomass,
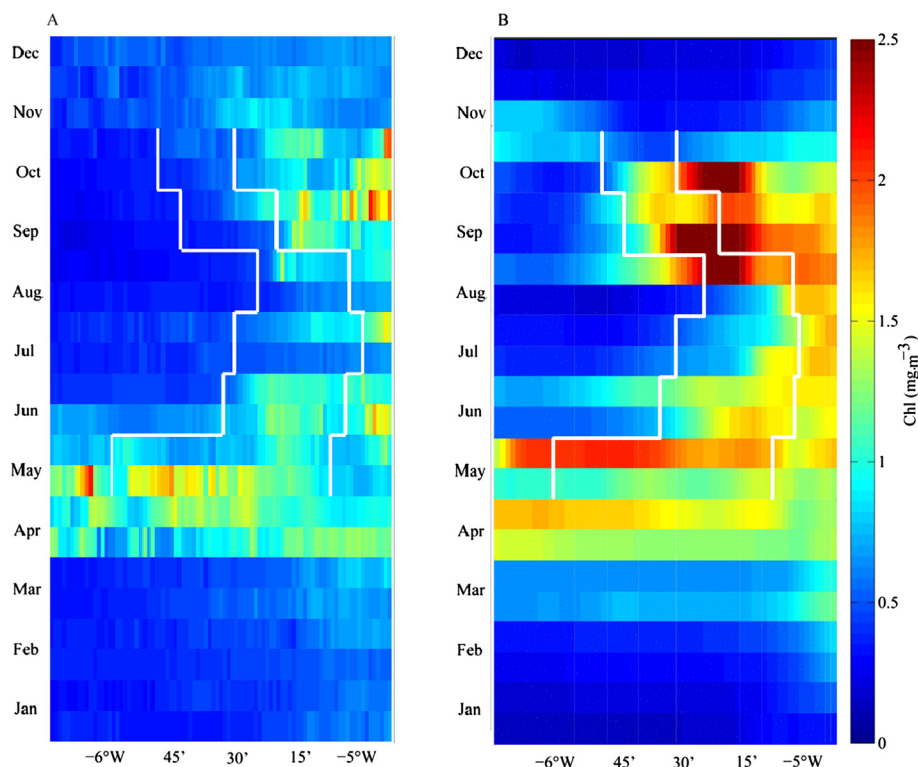

Fig. 9. Hovmöller diagram of seasonal evolution of surface chlorophyll concentrations along the 48°08′ N transect (see Fig. 1) (A) derived from satellite MODIS climatological data and (B) from model output (bi-weekly data). The white solid lines indicate the limits of the time-varying clusters computed from the *k-means* analysis (monthly averaged simulated physical fields). Only one cluster is defined over the whole modeled area (vertically homogeneous water column) during winter months (*i.e.* November to April). Between May and October, this area is separated in three distinct clusters (A to C on Fig. 4B).
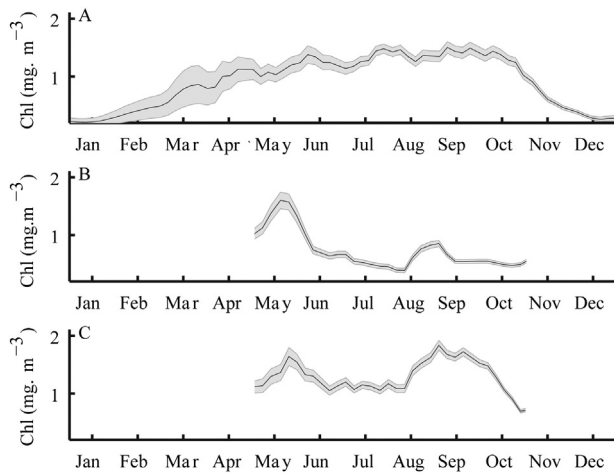
Fig. 10. Modeled seasonal evolution (running mean over an interval of 15 days) of surface chlorophyll concentrations spatially averaged over the three time-varying clusters: (A) well-mixed area (see cluster A in Fig. 4 for the summer period), (B) stratified area (cluster B) and (C) frontal area (cluster C). Black solid line is the average of five repetitions of the simulation and shaded area shows the standard deviation. Cluster B and C are defined only during the summer period (May to October).

Fig. 11. Relative contributions (%) of each plankton functional groups (red: diatoms, purple: Large Non Diatoms (LND), blue: Small Non Prochlorococcus (SNP) and green: *Prochlorococcus* sp.) to the total surface phytoplankton biomass ($gC \cdot m^{-3}$) averaged over (A) the well-mixed area (see cluster A in Fig. 4), (B) stratified area (cluster B) and (C) frontal area (cluster C). In each panel, solid line is the average value from five repetitions of the simulation and shaded areas show the standard deviation. Cluster B and C are defined only during the summer period (May to October). (For interpretation of the references to color in this figure legend, the reader is referred to the web version of this article.)

reaching ~75% in February and March (Fig. 11A). Indeed, the early spring phytoplankton bloom is initiated near shore in early February by the SNP group (4–5 mgC·m^{-3}) since it has more affinity for low light levels than larger cell size organisms (Fig. 12C).

From the end of March, the SNP group contribution undergoes a sharp decrease, passing from >70% to <35% of the total biomass (Fig. 11A). This collapse is coincident with the increase in large phytoplankton groups' biomass (mainly diatoms) and the presence of heterotrophic zooplanktonic grazers following the phytoplankton spring peak. Zooplankton biomass goes from <10 mgC·m^{-3} to >28 mgC·m^{-3} between March and the beginning of April (not shown). Diatoms become dominant from the beginning of April, when light-limitation no longer impedes their growth.

From May to October, the mixed area is however restricted to only the coastal waters, homogenized by tidal currents and offshore and frontal regions are distinguished by our clustering method. During summer, this coastal, tidally mixed area exhibits its higher phytoplankton biomass, (Fig. 9) mainly composed of large cell sizes, particularly diatoms with a biomass of 4–5 mgC·m^{-3} (Fig. 12A) and a ~45% contribution to the total carbon biomass (Fig. 11A); to a lesser extent LND contributes to 25–30% of total biomass with levels of 3–4 mgC·m^{-3} (Figs. 11A and 12B). Advantaged by their high growth rate, these large cells outcompete smaller phytoplankton cells in this nutrient-rich coastal mixed layer during summer. Between June and October, SNP accounted for only ~20–25% of total carbon biomass (Fig. 11A).

The decrease in available light in October leads to a progressive shift from large phytoplankton dominance (Fig. 11A) to winter conditions community dominated by SNP (~50% in December) which persists until the following year spring bloom in February–March.

3.3.1.2. Stratified offshore area. The offshore surface phytoplankton spring peak occurs later in the stratified part of the Iroise Sea (region B) than in the coastal area (region A) but is also initiated by small cell size groups whose biomass reaches 6–7 mgC·m^{-3} in March (Fig. 12C). This first bloom is followed in April–May by a peak in diatom biomass having a similar magnitude of ~8 mgC·m^{-3} (Fig. 12A). This diatom peak occurs concurrently with the establishment of seasonal stratification in this part of the Iroise Sea, which allows higher average irradiance levels in the shallowing surface layer. At this time, offshore surface phytoplankton biomass consists of ~35% diatoms and 35% small size cells (Figs. 11B and 12A and C). The remaining biomass
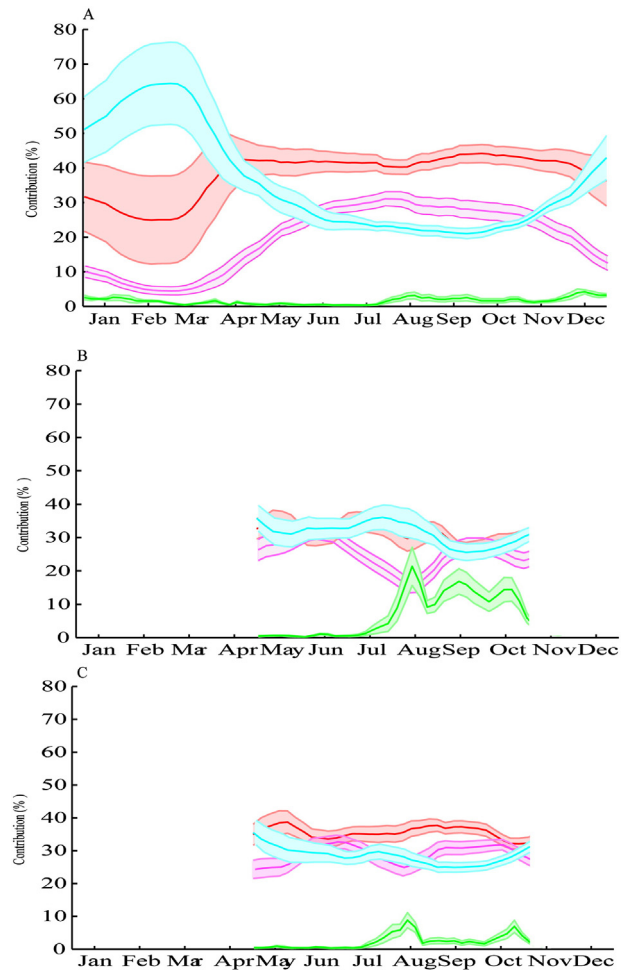
consists of the LND group that shows a slightly slower growth and reaches its maximum value offshore only in June (Figs. 11B and 12B).

During summer, low biomass in surface waters presents a high degree of coexistence between diatoms, LND and small cells (excepting *Prochlorococcus* sp. analogs), each of which accounted for ~30% (Fig. 11B).

Prochlorococcus sp. analogs are almost absent from the simulated phytoplankton community in the whole Iroise Sea ecosystem (Fig. 12D). Their proportion does not exceed few percent except in late summer at the surface of the stratified region (region B) where they account for 15–20% of total biomass from August to late October (Fig. 11B). Their growth during the rest of the year is limited by temperature and is also controlled by oxidized forms of nitrogen. Their presence is thus restricted to very oligotrophic waters west of the front with maximal temperature during late summer.

3.3.1.3. Frontal area. Similar to the offshore area, the frontal sub-region (region C) shows a high degree of coexistence from the late spring/beginning of the summer (Fig. 11C) during which total phytoplankton carbon biomass is intermediate between high chlorophyll in the mixed region and lower levels in the oligotrophic offshore surface waters.
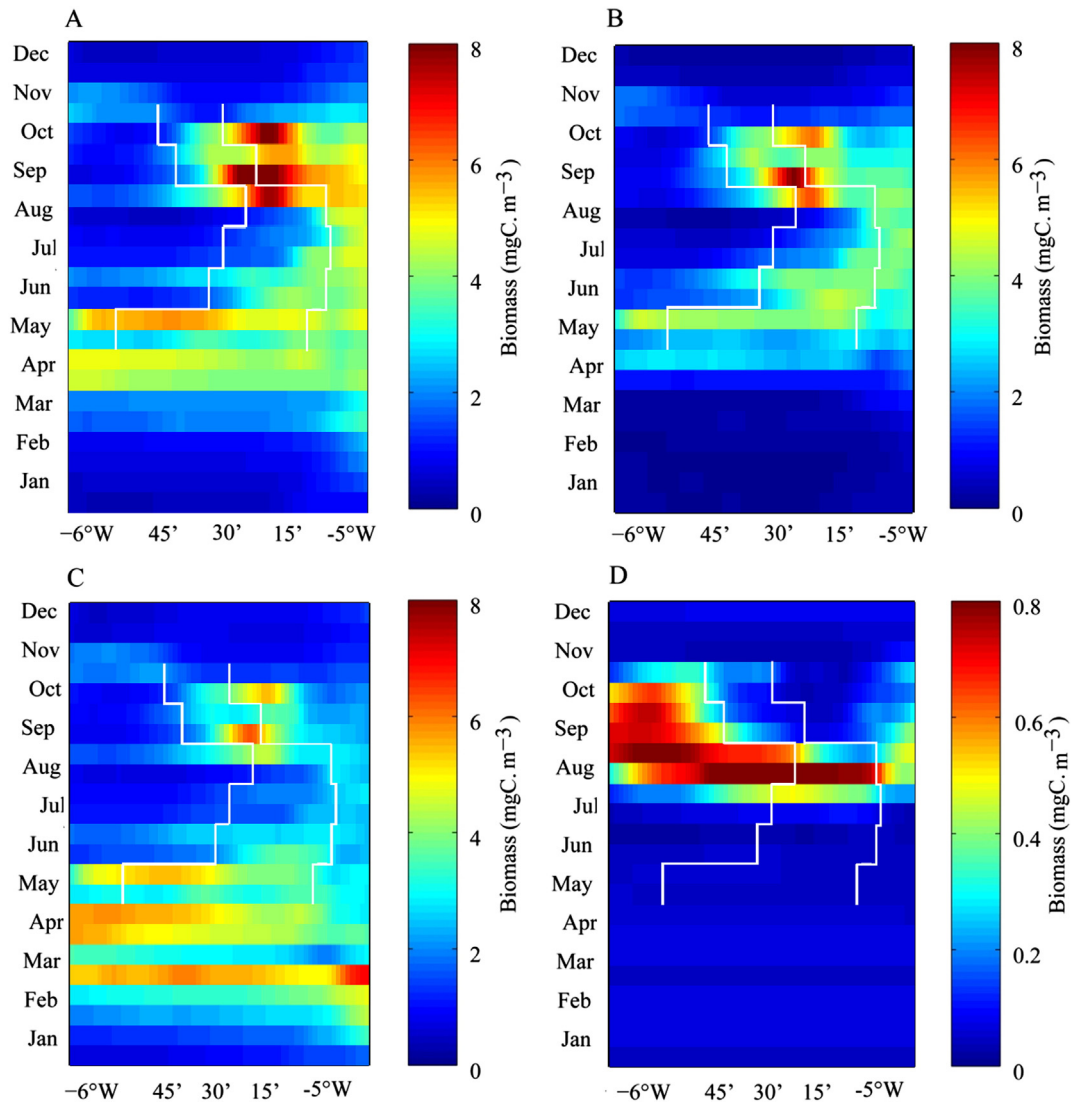
Fig. 12. Hovmöller diagram of modeled surface biomass of the four plankton functional groups along the 48°08′ N transect (see Fig. 1) (A) diatoms, (B) Large Non Diatoms (LND), (C) Small Non *Prochlorococcus* sp. (SNP) and (D) *Prochlorococcus* sp. The white solid lines indicate the limits of the time-varying clusters computed from the *k-means* analysis (monthly averaged physical fields).

However, in September–October, the modeled frontal region is the one with the highest phytoplankton carbon biomass (20 mgC·m^{-3} Figs. 9B and 12A, B and C), mainly composed of diatoms (up to 40% of the total phytoplankton biomass; Fig. 12A). This maximum at the simulated front is not represented in satellite data in which the front is located eastward with highest phytoplankton biomass nearshore.

3.3.2. Vertical distribution

The vertical distribution is also different between the four functional groups. Fig. 13 shows the modeled vertical profiles of the groups' contributions to total phytoplankton carbon biomass along the 48°08′ N transect (August–September average). Compared to region A in which large size cells are the most abundant, the deep chlorophyll maximum of the stratified area (region B) is composed of 45–50% SNP (Fig. 13C). This group is also dominant below the DCM depth of the stratified, offshore water whereas its relative contribution decreases to the east. Conversely, diatoms and LND show increasing contributions from open waters to the coastal part of the Iroise Sea.

3.3.3. Observational data comparison

The community composition derived from *in-situ* SOMLIT data (Fig. 14) can be compared with that of homogeneous coastal waters (cluster A; Fig. 11A). In agreement with model results, the annual cycle of total phytoplankton biomass (Fig. 14A) is characterized by a spring peak (April) followed by high phytoplankton concentrations during the entire summer season. As previously noted, despite a similar order of magnitude, the modeled phytoplankton biomass in the coastal region is slightly higher than *in-situ* levels from SOMLIT dataset (Fig. 14A), especially during the end of the summer (September–October).

In general, the relative contribution of each functional group to the total biomass is lower in amplitude and smoother in temporal variations in our simulations than it does in the real environment (Figs. 11A and 14B). *Prochlorococcus* sp. cells (PLP in our simulations) were not detectable in flow cytometry samples. They are therefore not present in Fig. 14B. In the same way, they are absent in model output in the coastal area. However, this modeled PLP group becomes more significant when waters become warm and oligotrophic (~15% of contribution to the total biomass), during summer time in offshore surface waters. Unfortunately, the lack of available offshore data does not allow validation of this assessment.

The group formed by picoeukaryotes and *Synechococcus* sp. (SNP, Fig. 14B) fits in its distribution with our modeled SNP group; observed concentrations exhibit their highest relative contribution during the winter, rising up to 80% of total carbon biomass in January and February
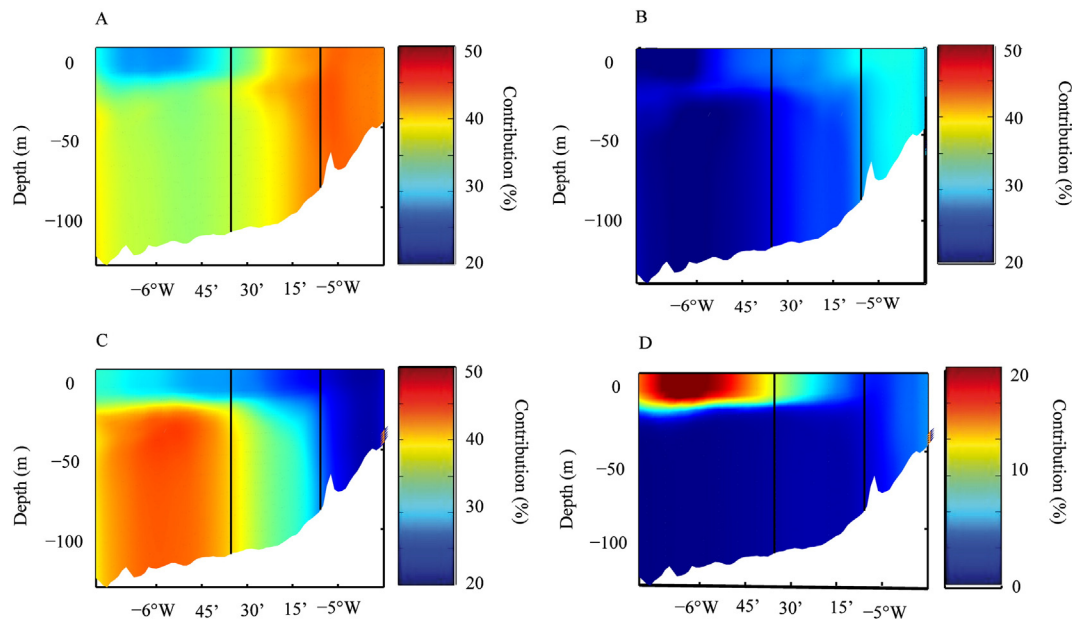
Fig. 13. Vertical distribution of the contribution (%) of each plankton functional groups to the total carbon biomass (mgC·m^{-3}) along the 48°08′N transect (see Fig. 1) in August–September (two months average) (A) diatoms, (B) Large Non Diatoms (LND), (C) Small Non *Prochlorococcus* sp. (SNP) and (D) *Prochlorococcus* sp. The contours of the three sub-regions coming from the *k-means* clustering analysis (computed from August–September averages of physical fields) are drawn on each panel (black lines).

in SOMLIT data. In model results, the relative contribution of SNP is of the same order of magnitude of ~75% (Fig. 11A). At the SOMLIT station, this population displays a sharp decline, falling to <10% in April as larger groups show increasing levels from the beginning of March. In late spring and during summer, the contribution of small size to total biomass is lower than 10% and increases from August to the end of October, reaching ~50% of total biomass in late November. This annual cycle of small size cells is in good agreement with model output corresponding to the coastal mixed region (Fig. 11A) although the extent of the decrease in proportion in spring is smaller in our model. Indeed, SNP contributes about 20% of total biomass in summer, which is slightly more than in SOMLIT data. From March to August, diatoms are dominant in percentage of biomass in both model (40%) and *in-situ* measurements (40%) but with large oscillations (between diatoms and LND) observed in natural system during spring that are not present in modeled system (Fig. 11A).

As the distinction is made between nanoplankton and dinoflagellates (LND group) in observational data, we can assess their succession in time. The dynamics of nanoflagellates and dinoflagellates are fully coupled during the winter and spring bloom and a decoupling can be observed after June with a dominance of dinoflagellates over smaller cell size, especially from July to October.

Among large cells, a shift from the dominance of diatoms (70% between May and August) to dinoflagellates (35–40% from mid–August to October) is observed in late summer in SOMLIT natural assemblages and is not represented by our model.

4. Discussion

4.1. Model skill assessment

A regional configuration of a circulation model (ROMS-AGRIF) coupled to a phytoplankton-diversity model (DARWIN) has been used to simulate a realistic seasonal cycle of the Iroise Sea phytoplanktonic communities. Our model, when compared to satellite and *in-situ* data, properly represents the overall seasonal variations as well as the spatial heterogeneity of physical and biogeochemical conditions. A biogeography of the Iroise sea ecosystem can be established during the summer season along an east to west gradient. Indeed, from May to October,

our model displays three hydro-dynamically different sub-regions ranging from (i) fully-mixed waters nearshore to (ii) stratified waters off-shore due to shallowing of the summer mixed layer and (iii) the Ushant tidal front that separates the first two. In response to this environmental variability, the total chlorophyll concentrations display contrasting distributions with a maximum at the surface of the frontal area, intermediate levels in the coastal well-mixed region and a subsurface maximum (DCM) in the offshore area (Fig. 5).

Nonetheless, some biases exist between model results and observational data. Among them, the depth of the DCM in the offshore region is shallower in our simulation than in the *in-situ* data. This bias is consistent with a modeled thermocline that is shallower than its observed counterpart (Fig. 4C).

A westward zonal shift in the simulated surface front position is observed when compared to climatological satellite data (see SST in Fig. 4 and the consequent shift in Chl in Fig. 5). Along the 48°08′ N transect, the Ushant front is thus located at ~5°15′ W in satellite observations (see for example Figs. 4A and 9A) and at ~5°30′ W in model outputs (see Figs. 4C and 9B). This shift in the front location is linked to the biases of the physical circulation model (*e.g.* boundary conditions *etc.*) and does not impact the results discussed in this study. Indeed, while being shifted zonally, the front location corresponds to the maximum temperature gradient together with the surface chlorophyll maximum in both the satellite (Figs. 4A, 5A and 9A) and the model outputs (Figs. 4B, 5B and 9B). The three resulting hydrodynamical provinces of the Iroise Sea (*i.e.* stratified, frontal and well-mixed regions) during summer are thus correctly represented by the model.

Moreover, our simulations slightly overestimate NO_3 concentrations while slightly underestimate PO_4 and SiO_2 when compared to the 2007 and 2009 data obtained from hydrographic cruises (FroMVar). This bias may result from the nutrient boundary conditions applied [Sourisseau, pers. Comm.] which display an NO_3 over PO_4 overestimation. Indeed, those boundary conditions derive from a large, historical dataset and discrepancies exist between that dataset and the 2007–2009 FroMVar cruises dataset used for evaluation of the longitudinal section.

Another visible difference between model results and observational data is an overestimation of modeled chlorophyll levels in high-concentration areas when compared to both *in-situ* and satellite data. Underestimation of chlorophyll concentrations observed in the satellite-derived
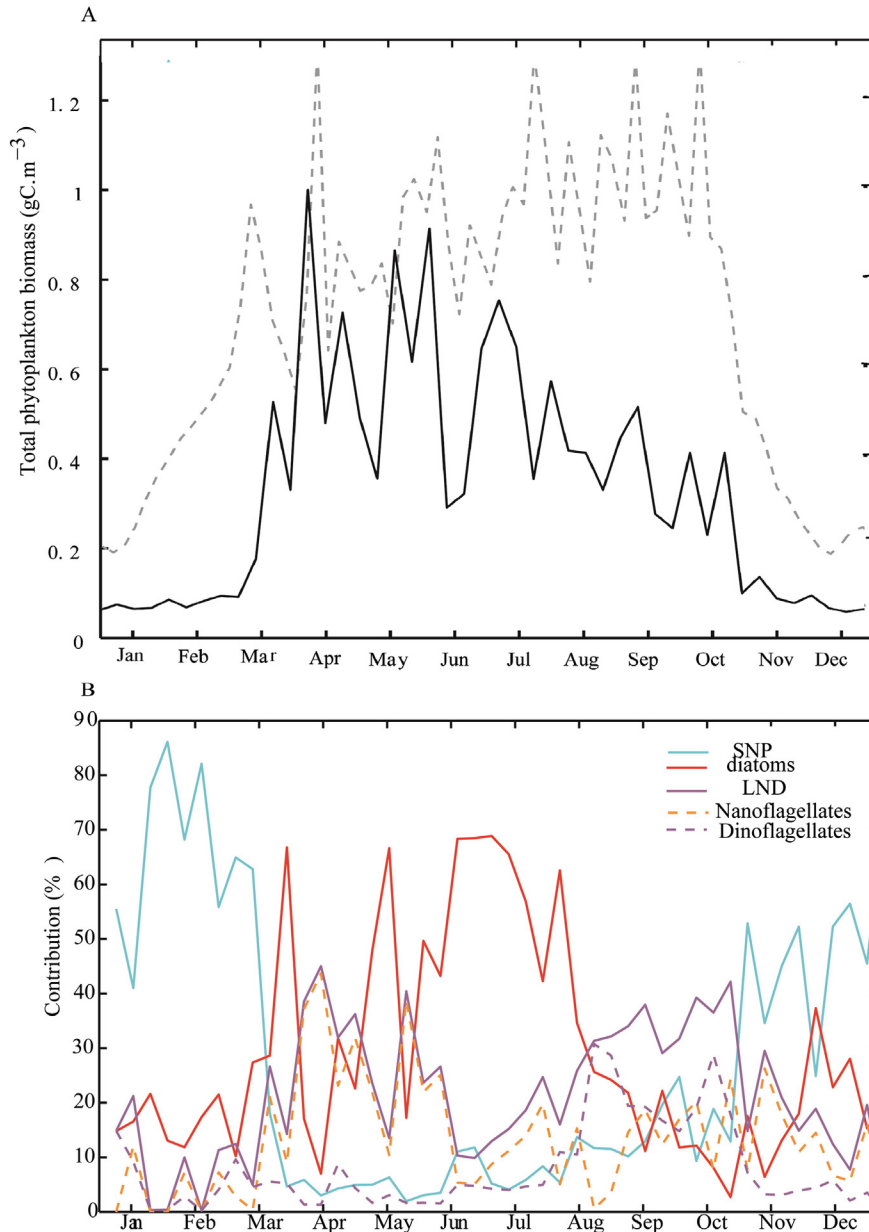
Fig. 14. (A) Seasonal evolution (5 days average) of total phytoplankton biomass at SOMLIT Brest station (Ste Anne du Portzic (48°21′ N; −4°33′ W) (solid black line) and in the surface layer of the modeled well-mixed area (cluster A; dashed black line). (B) Composition of the phytoplankton assemblages in SOMLIT data (% of total biomass) (solid blue line: picoeukaryotes + *Synechococcus* sp., solid red line: diatoms, solid purple line: nanoflagellates + dinoflagellates, dotted orange line: nanoflagellates only and dotted purple line: dinoflagellates only). These curves are obtained by compiling different years of data (1998 to 2012). (For interpretation of the references to color in this figure legend, the reader is referred to the web version of this article.)

could be explained by the post-processing used to eliminate the signal due to non-phototroph organic matter from total chlorophyll *a* (Gohin et al., 2002). Similarly, an underestimation of chlorophyll levels computed with the same algorithm from the SeaWiFS sensor, compared to *in-situ* measurements, has been reported by Gohin et al. (2008) in turbid waters along the coast of the French Atlantic continental shelf.

However, comparison with *in-situ* data also suggests that the model overestimates chlorophyll concentrations, which means that this chlorophyll bias is not only due to the approximations made by the satellite's post-processing. Furthermore, this overestimation of the modeled chlorophyll corresponds to an underestimation of simulated vertically-integrated primary production in the well-mixed coastal waters during the summer (Fig. 7). Indeed, Videau (1987) reported daily production rate as high as 3500 mgC·m^{-2}·day^{-1}, more than twice the values obtained in our model for the coastal area (~ 1500

mgC·m^{-2}·day^{-1}). Their study shows closer results with our modeled values in the other areas of the Iroise Sea with field values of primary production of 1660–1800 mgC·m^{-2}·day^{-1} at the Ushant front and 885 mgC·m^{-2}·day^{-1} in the stratified offshore surface waters. Along with chlorophyll and primary production, the assimilation number is consequently underestimated by the model in the very productive coastal waters. Indeed, despite qualitatively similar patterns with lowest values in the frontal area and maximum values in the well-mixed coastal region, Videau (1987) reports significantly higher values of assimilation number (10.7 mgC·mgChl^{-1}·h^{-1} in the coastal domain) when compared to our model output (Fig. 8A).

The C:Chl ratio used in the model may explain these differences between the simulations and field measurements. Firstly, the coastal area is, during summer, primarily dominated by microphytoplankton especially diatoms (>40%). Indeed, this group is assigned, together with

the highest maximum intrinsic growth rate, the lowest C:Chl ratio (50 mgC:mgChl^{-1}) among the four plankton functional groups (see Appendix A). This relatively low C:Chl ratio, which is in the lower range of literature values for diatoms (Osmond et al., 1995) may cause the carbon:Chl underestimation in this region.

In addition, the use of a fixed C:Chl ratio within each group does not take into account the sensitivity of this ratio to light variability. Indeed, the C:Chl ratio generally increases with increasing PAR (Geider, 1987; Geider et al., 1997), which is relatively high in the coastal shallow waters of the Iroise Sea. Noticeably, chlorophyll levels are however underestimated by the model compared to *in-situ* data at DCM depth of the western stratified side of the front (Fig. 5, C and D) where low light might lead to a decrease C:Chl ratio in nature (not represented by our model).

Finally, dinoflagellates that are known to have a very high C:Chl ratio (Chan, 1978, 1980) are very abundant at the end of the summer in coastal waters in observational data (~35–40% of the total biomass in SOMLIT data; Fig. 14, B) but are only present in significantly lower proportions in the model results (~15–20%). This lower contribution of modeled LND compared to the *in-situ* measurements may also explain in part the low effective C:Chl ratio on the model compared to data in the coastal region in September–October.

In the two following sections, results which emphasize the complex biophysical interactions that take place in the Iroise Sea during a seasonal cycle will be discussed in light of their potential to significantly affect the phytoplankton biomass and composition.

4.2. Seasonal succession

From November to April, a deep mixed layer characterizes the whole domain. Here we discuss the phytoplankton composition in the entire study area prior to the offshore stratification, which develops in May.

In late winter and early spring, the phytoplankton community of the Iroise Sea is largely dominated by picoeukaryotes and *Synechococcus* sp. (SNP). The reason for dominance of SNP at the expense of larger size cells in the early biomass maximum is their lower light optimum. On average over the whole domain, this small size class has the maximal fitness (minimal R*) from November to March (Fig. 15A). Therefore, the high-mixing conditions maintained during the winter causes light-limitation of phytoplankton growth, especially for light-stressed large cells, and leading to a competitive advantage for small cells (SNP). Therefore, the proportion of the picoplankton cells is about ~50% of total biomass from November to the end of December and it experiences rapid development as daylight increases (from the beginning of January) to rise to almost 80% in February. This increase occurs earlier in the coastal part of the domain (Fig. 9) than in offshore regions. Indeed, as long as the whole water column is vertically homogenized across the whole area (*i.e.* until the stratification takes place offshore in late April), the vertically averaged PAR in the mixed-layer is highest in the coastal region in waters shallower than 100 m.

Indeed, the onset of the phytoplankton bloom in the offshore waters of the Iroise Sea progresses more slowly due to enhanced light limitation (Fig. 16) with maximum biomass coincident with the establishment of seasonal stratification in April–May.

Afterward, as irradiance continues to gradually increase, larger phytoplankton peaks. The diatom contribution increases from ~20–25% in early March to >40% in early April. The other large phytoplankton group (LND) also increases from <10% in March to a peak of ~30% in late May (Fig. 12B); they become the functional group having the highest mean fitness in April (Fig. 15A). This succession of dominant phytoplankton types (SNP to diatoms (and LND)) takes about one month (between March and April) to occur which is in agreement with SOMLIT data (Figs. 12 and 14B). In those data, diatoms and LND follow the same trend going respectively from 10 to 60% and 5 to 40% of total carbon biomass. This shift in the community during spring has been described by Rees et al. (1999) in an area located northwest of

our domain, at the Celtic Sea Shelf Edge. Their results have shown that picoplankton (<2 μm ESD) was responsible for almost 50% of the phytoplankton biomass and 42% of the primary production in late winter followed by a significant increase of the larger cells growth and a sharp decline in smaller organisms between the end of March and April 1994. In their study and in agreement with the modeled succession here, the change from small nanoflagellates and picoplankton (roughly comparable to the modeled SNP group) to larger phytoplankton (equivalent to diatoms and LND groups) occurs as soon as the water column stabilized. Therefore, modeled succession timescales (~1 month) are similar to the observations of succession in natural assemblages. Indeed, as soon as light becomes sufficient for large phytoplankton growth and in the absence of nutrient limitation, resource competition becomes advantageous for large plankton phenotypes (*i.e.* opportunistic, r strategy), owing to their higher specific growth rate under nutrient-saturated conditions.

4.3. Phytoplankton summer biogeography

During summer, the dynamically-driven spatial heterogeneity of the physical and chemical environment (mainly light and nutrient levels) leads to specific patterns of total phytoplankton biomass as well as community composition in terms of functional groups.

4.3.1. Coastal mixed area: r-strategy dominance

In the fully mixed and nutrient rich near-shore sub-region, large phytoplankton types (diatoms and to a lesser extent LND) are dominant (~55% of the total biomass) in both modeled and *in-situ* communities (Figs. 12A and 14B).

The diatom contribution alone represents ~35–40% of the total phytoplankton carbon biomass simulated by our model (Fig. 11A). In the same way, the SOMLIT community is dominated by diatoms until mid-August (and by dinoflagellates later, for reasons detailed below). During the September 2009 FroMVar cruise, microphytoplankton accounted for 30–50% of biomass in the well-mixed nearshore region (Landeira et al., 2014), which is a similar magnitude as in our model results.

Diatoms and LND are the groups with the lowest R* (Fig. 15A) in the coastal well-mixed area between March and October. In this region, ambient PO$_4$ concentrations exceed the minimal equilibrium resource concentration of the whole phytoplankton community R$^*_{min}$, (Fig. 17). This suggests the absence of nutrient limitation in this well-mixed area during the summer. Moreover, semi-diurnal and spring/neap tides cycles (Maguer et al., 2011) make the mixing highly variable at temporal frequencies of hours, days or weeks over the continental shelf. Among this tidal variability, the spring/neap tides cycles occur with a time frequency of ~15 days and potentially affects the phytoplankton growth as its time-scale matches the phytoplankton generation time of few days. Indeed, nutrient pulses, combined with better light conditions due to de/restabilization (*i.e.* variations of the mixed layer depth during tidal cycles) may also promote opportunistic phenotypes (diatoms). Therefore, the presence of this non-stationary environment is likely to allow fast-growing, r-strategy phenotypes (diatoms) to quickly outcompete phenotypes with lower growth rates (Cadier et al., subm.) in the same way that it has been observed on larger time scales at high latitudes (Dutkiewicz et al., 2009). Similar to their results, our model exhibits a decoupling between ambient nutrient concentrations (shown here for PO$_4$ but it has been tested for NO$_3$ and SiO$_2$ with the same conclusion) and R$^*_{min}$ (Fig. 17) in the coastal well-mixed sub-region.

Diatom dominance ends in the SOMLIT observations in late August/early September when the LND group becomes dominant (Fig. 14B). This observed shift toward dinoflagellates (LND) dominance is however not simulated by our simulations in which diatoms are more competitive than other large size analogs all summer long and until the end of November. This discrepancy could be due to the common ability of dinoflagellates to use heterotrophic forms of organic matter
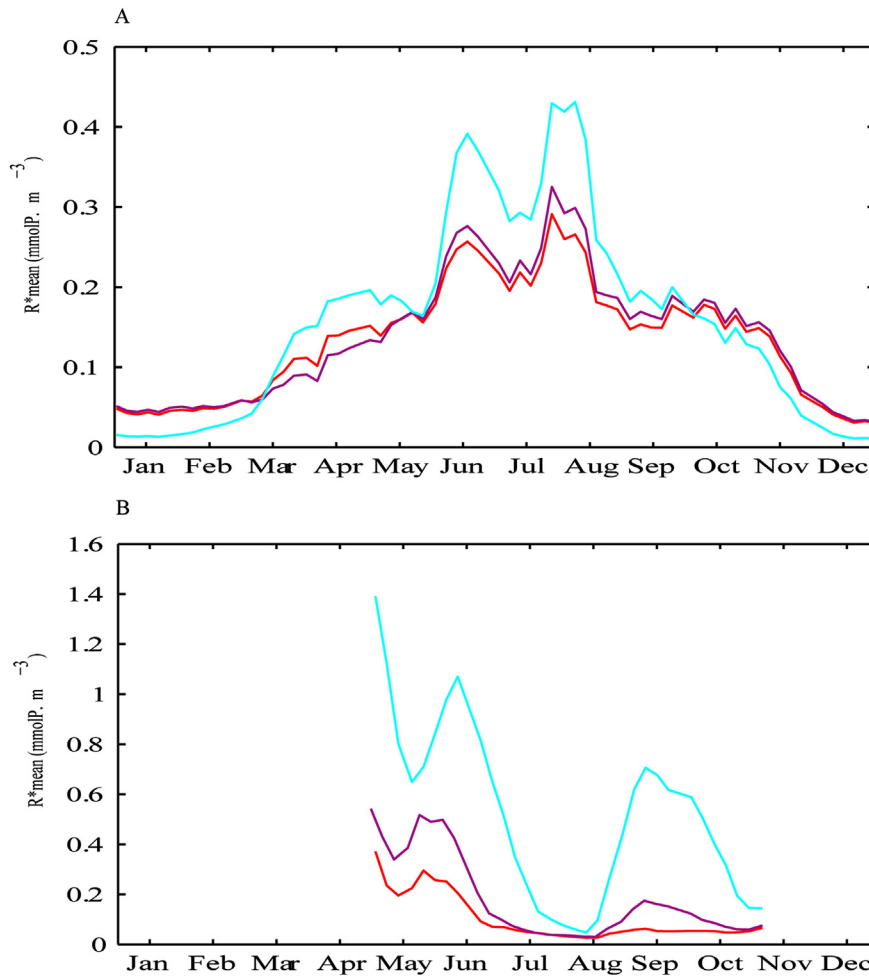
Fig. 15. Time series of biomass-weighted average R* for PO₄ computed for each functional groups (red: diatoms, purple: Large Non Diatoms (LND) and blue: Small Non *Prochlorococcus* sp. (SNP)) averaged over the surface mixed layer of (A) the well-mixed area (see cluster A in Fig. 4) and (B) stratified area (cluster B). (For interpretation of the references to color in this figure legend, the reader is referred to the web version of this article.)
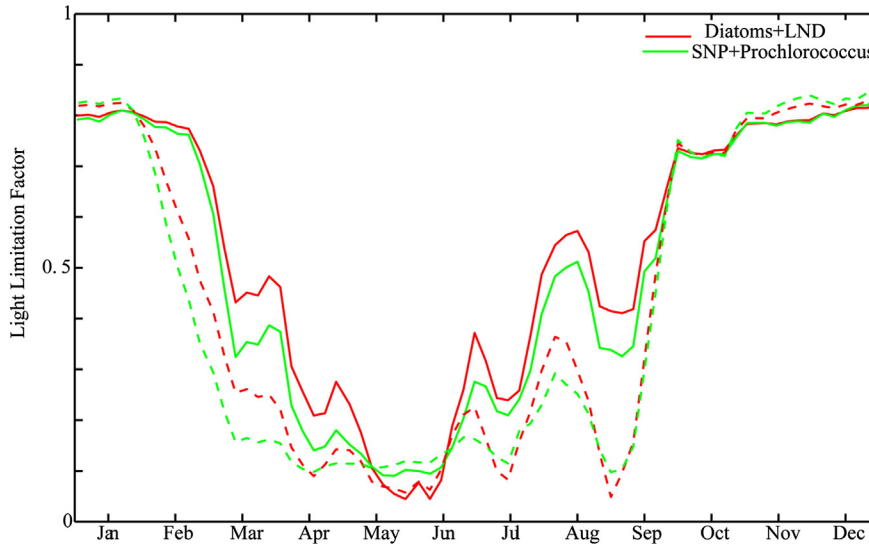

Fig. 16. Seasonal evolution of a dimensionless light limitation factor, ranging from 0 (no inhibition) to 1 (complete limitation of growth by light), experienced by large (DIAT + LND: red) and small (SNP+ *Prochlorococcus* sp.: green) phytoplanktonic functional groups (these curves were obtained by averaging the light limitation factors of each phenotypes within each functional groups). This factor is plot for station 1 (48°08′ N; −6°10′ W; solid line) and station 3 (48°08′ N; −4°45′ W; dashed line) of the 48°08′ N transect (see Fig. 1). (For interpretation of the references to color in this figure legend, the reader is referred to the web version of this article.)
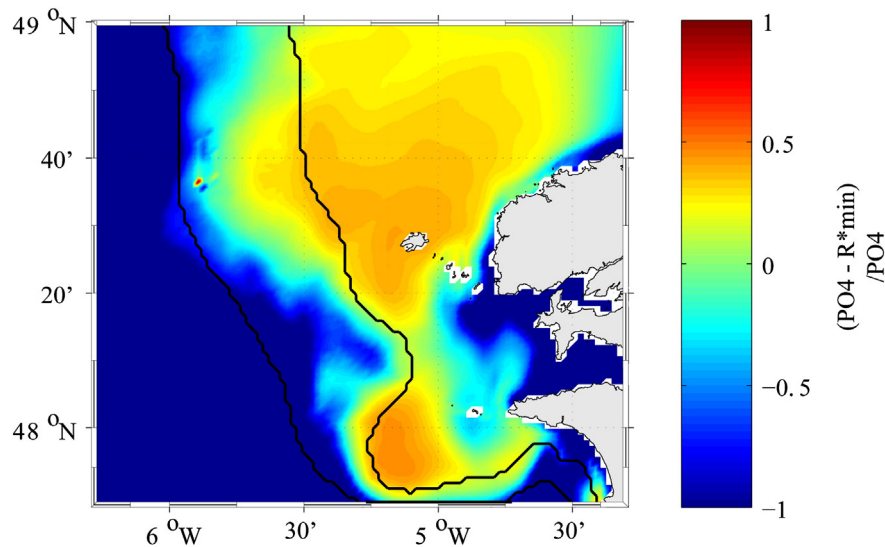
Fig. 17. Relative difference between diagnosed R^*_{min} and ambient phosphorus concentrations $(PO_4 - R^*_{min}) / PO_4$ in the surface layer during the summer (August–September average).

(phagotrophy and osmotrophy) as nutrients and light become limitative for phototrophic growth (Mitra and Flynn, 2010; Flynn et al., 2012). Mixotrophy was not included yet in the model and is probably a key feature which could lead to higher fitness of mixotrophic flagellates that are modeled in higher proportions in postbloom conditions. Besides mixotrophy, the direct comparison between SOMLIT observations and the modeled coastal sub-region also involves a spatial extrapolation of a punctual observation to a whole region; this extrapolation of a discrete event may explain some differences between *in-situ* data and model output.

4.3.2. Stratified offshore surface area: enhanced coexistence between plankton functional types

On the western side of the Ushant front, the contribution of the summer simulated picoplankton (SNP and *Prochlorococcus* sp. analogs) in surface oligotrophic stratified waters reaches ~35–40% (Fig. 11B) which is approximately two times the one of the well-mixed coastal region. Indeed, although offshore surface waters have optimal light conditions, they encounter oligotrophic conditions during the summer. The nutrient limitation is emphasized by R^*_{min} values that are either similar to the ambient nutrient concentration (with a ratio of $(PO_4 - R^*_{min}) / PO_4$ close to zero) or lower than the available resource ($0 > $ ratio > -1) at the surface (Fig. 17). Despite their higher maximum growth rate, large cells are further nutrient-limited than smaller ones, resulting in similar effective growth rate for both size-classes. In our simulations, this similarity leads to an enhanced co-existence between large and small cell sizes (from both SNP and *Prochlorococcus* sp. groups) that are found in similar proportions in offshore surface waters (Fig. 11B). Indeed, oligotrophic conditions enhance co-occurrence between groups having different growth strategies (r and K) by decreasing the invasion rate of fast-growing larger phenotypes and allowing low maximum growth rate/high nutrient affinity picophytoplankton to remain in significant proportion in the total biomass.

Nonetheless, despite their control by low nutrient levels, the average equilibrium resource concentration R^*_{PO4} is lowest for large phytoplankton (diatoms and LND) in the oligotrophic surface layer on the stratified side of the Ushant front between June and August (Fig. 15B). This result is explained by the strong grazing pressure applied to small phytoplankton cells by microzooplankton. Indeed, the averaged proportion of small cells inside the total zooplankton diet is 61.51% during August–September in the mixed layer of the stratified area compared to only 27.19% in the well-mixed coastal area wherein the mixed layer depth exhibits strong variations (associated with the neap/spring tide

cycle). The consequent mortality rate of picoplankton by predation tends to increase their equilibrium resource R^* and prevents the dominance of this group in surface oligotrophic waters.

Samples from the surface west of the front revealed effectively a higher dominance of small (<10 μm) cells at the surface ranging from 61 to 80% (Schultes et al., 2013). Moreover, earlier studies already measured large amounts of small phytoplankton cells (nanoflagellates) in the stratified waters west of the Ushant front (Pingree et al., 1978; Le Corre and L'Helguen, 1993). Therefore, our model tends to underestimate the proportion of small phytoplankton (SNP and *Prochlorococcus* sp. analogs) and to overestimate the degree of coexistence between the two size-classes through an excessive effect of zooplankton grazing in the control of the small cells population. A second explanation relates to that the different grouping method used to assign species to functional groups for the model and the observations. Modeled picoplankton is restricted to cells smaller than 1 μm ESD and part of the nanoplankton (between 2 and 20 μm) therefore belongs to the group of 'Large Non Diatoms' cells (dino- and nano-flagellates; 10 μm ESD) in the model. This choice of parameters may induce the following bias: among small phytoplankton reported at the surface in the stratified side by previous field studies, nanoplanktonic cells, flagellates in particular, are part of the LND functional class in our model classification. This last point raises a key issue for studies of phytoplankton communities and for comparisons between field-based, laboratory-based and model experiments data. Indeed, the choice of criteria defining functional types used to aggregate species in terms of size or function can be partly inconsistent between different studies.

4.3.3. Deep chlorophyll maximum on the stratified side of the front

The SNP group (*Synechococcus* sp. analogs and picoeukaryotes) exhibits its highest contribution to the total biomass within the DCM in the stratified waters offshore of the front, as well as in deeper waters with a proportion of ~40–50% (Fig. 13C). Their success results from their high affinity for low light levels.

Conversely, *Prochlorococcus* sp. analogs reach their highest proportion (15–20%) in warm and oligotrophic surface waters and are almost absent in deeper waters despite their high affinity for low light. Their absence in deeper water is mainly due to their low affinity for low temperature. Moreover, the presence of sufficient nutrients, especially oxidized forms of nitrogen, at DCM depth benefit other small size group (SNP). According to field measurements, the vertical distribution of prokaryotic picoplankton is different between *Synechococcus* sp. and *Prochlorococcus* sp. Indeed, *Synechococcus* sp. are usually found in

surface and sub-surface waters whereas *Prochlorococcus* sp. are preferentially observed deeper, in the deep chlorophyll maximum of stable oligotrophic area of the ocean (Casotti et al., 2003; Olson et al., 1990). However, this distribution is not simulated by our model, which shows the inverse vertical pattern, as it does not distinguish phytoplankton phenotypes in terms of pigment composition and differential light absorption spectra.

4.3.4. Phytoplankton functional type composition in the Ushant tidal front

Just as in the stratified area, the model simulates a high degree of coexistence between the three functional groups (*i.e.* SNP, LND and diatoms) at the Ushant Front. At this location, large opportunistic cells experience a limitation of their fast growth rate by low surface light levels of ~100 W·m^{-2} (self-shading, Fig. 8, B), which allows phytoplankton with lower maximum growth rates but less instantaneous nutrient limitation (picoplankton) to maintain a similar biomass. This process of self-shading may also produce the minimum of productivity per unit biomass (assimilation number) simulated at the position of the Ushant Front (Fig. 8A), in accordance with Videau (1987) work.

The Ushant front thus exhibits functional group composition that is intermediate between the two other sub-regions: it does not particularly differentiate itself by a significant modification in the proportion of any given functional group. This may be the result of the highly dynamic behavior of the tidal front and resulting horizontal mixing. The frontal sub-region identified by our clustering method results from a two-month time average during the August–September period. In reality, the exact front position is a very dynamic feature which moves zonally at different timescales. At seasonal scale, its position is closer to the coast in July (South; 5° W) or beginning of August (North; ~5°30′ W) and moves westward from August to October (6°15′ W at the end of October) (see Fig. 9 and Cambon (2008)). An additional, higher frequency, variability is the tidal cycles with periods of few hours (semi-diurnal cycle) to ~15 days (spring/neap tides cycle). These temporal fluctuations in the frontal environment would not allow competitive exclusion or acclimation processes to take place in a way to isolate a specific community in the frontal area as these mechanisms occurs at slower time scale than the short residence time of water masses in the frontal area. Conversely, one can suppose that numerous exchanges with the surrounding waters contribute to the maintenance of a diverse community inside the Ushant Front, with a high degree of coexistence between functional groups of the same type as that observed in waters of the stratified side of the front. The results of Landeira et al. (2014) based on this cruise also illustrate these horizontal exchanges because no differences in the diatom species diversity were found in each of the three sub-regions. However, present results show only the composition in terms of functional groups and further investigation at the 'species' (*i.e.* phenotype) level are presented in a companion study (Cadier et al., subm.).

5. Conclusion

This study is the first biogeochemical modeling description of the Iroise Sea pelagic ecosystem. Our main goal was to evaluate how contrasted hydrodynamical regimes constrain the phytoplankton community at the regional scale in the vicinity of a tidal front. To investigate these influences, a self-assembling phytoplankton community model has been used. Biogeography and temporal dynamics of four major autotrophic groups, comprising a large number of phenotypes, have been simulated in the highly dynamical and contrasting environment of the Iroise Sea. This first part of our study has been dedicated to the description and validation of biogeochemical patterns and group composition (a second paper will be devoted to the description of the phenotypic diversity within the same simulations).

In terms of physical and biogeochemical properties, our model successfully simulates the different regimes of the Iroise Sea. Despite some aforementioned bias in absolute Chla concentration, which is probably due to missing processes in our model (such as variable

C:Chl ratio), it is undisputed that our model simulates three clear subregions that display significantly different total chlorophyll patterns in agreement with observed structures from both satellite-derived and *in-situ* observational data. We demonstrated that phytoplankton communities in the Iroise Sea experience significant variations from the winter to summer season and along a zonal, cross frontal gradient in environmental conditions. As already suggested and discussed by several studies (Sverdrup, 1953; Hutchinson, 1961; Huisman et al., 2004), vertical mixing plays a primary role in phytoplankton standing stock, primary production and species interactions as well as the composition of the phytoplankton community. By governing fluctuations in light and nutrient availability fluctuations, spatial and temporal variability in the mixed layer depth is shown to control the relative contributions of the four functional groups to the total biomass in the Iroise Sea macrotidal ecosystem. A deep mixed layer provides a high nutrient supply but low average levels of light favoring smaller, low-light adapted species during the winter and in the early spring bloom. Conversely, the limited mixing that occurs in the summer within stratified waters of the Iroise Sea (west of the Ushant Front) results in a nutrient-depleted offshore surface layer having low-biomass and the coexistence of diatoms, flagellates and small size species with high-nutrient affinity. This coexistence between functional groups is enabled by a combination of bottom-up (resource competition and limitation of large cells growth by nutrients) and topdown processes through the control of small phytoplankton biomass by microzooplanktonic grazers.

Over the continental shelf, water masses continuously mixed by tides all year long show a higher degree of competitive exclusion in favor of opportunist, fast growing species during the summer. This is likely to occur as nutrients levels are maintained at relatively high levels by vertical mixing due to strong tidal currents. In this coastal region, the effect of the high frequency variability linked to tidal cycle might also exerts a second order (but significant) control of water column stability, growth conditions and thus phytoplankton community composition, which is, on the first order (on average), dominated by diatoms. This aspect has not been addressed in this study that focuses only on seasonal cycle and will be address in subsequent study.

The frontal region is the most productive during the summer season but is associated with lower carbon fixation rate per unit of biomass than adjacent water masses because of self-shading (light limitation) experienced by large cells. This area does not show any specific composition in terms of functional group contributions to total biomass and constitutes an intermediate community between the mixed and stratified waters on either side of the front, probably due to horizontal mixing processes.

This study thus provides new knowledge about the heterogeneous distribution of the phytoplankton functional diversity in the Ushant Front environment by shading light over the link between dynamical parameters and the ecosystem structure. Despite its focus on the Iroise Sea, this work highlights processes that may well be significant in a wide range of regional domain.

The functional diversity resulting from those highlighted processes (backed by observations in the Iroise Sea) can however be refined by a comprehensive study addressing the diversity at a phenotypic level, which will be done in a companion paper. One can suppose that the qualitative attributes of the co-existing phenotypes and their functional traits might influence the resource use efficiency and contributes to the resilience and overall functioning of the ecosystem. In addition to functional traits addressed in this study (light, nutrients and temperature sensitivities), some complementary phytoplankton attributes and processes such as differential photo-adaptation through pigments composition or variable C:Chl ratios should be further considered for their potential impacts.

Finally, our results support the need for a better characterization of this functional diversity in field measurements with, in particular,

sampling strategies acknowledging a wider range of ocean dynamical variability frequencies (*e.g.* tides).

Acknowledgments

Appendix A

Table A1

Model parameters ($Z1$) microzooplankton, ($Z2$) mesozooplankton, (j) prey index (*i.e.* single phytoplankton phenotypes or microzooplankton). The origin of each parameter is indicated in brackets (superscript): (a) Follows et al., 2007; (b) Goebel et al., 2010; (c) field data; (d) adjusted for this study.

Param	Signification	Value	Unit
dts	Time step (t + 1 − t)	100	s
npmax	Phytoplankton numbers	120	n.d
C_{ext}	Phytoplankton subsisting threshold	1.10^{-6}	mmolP·m^{-3}
R_NP	N:P	16	mol/mol
R_SiP	Si:P	16	mol/mol
R_C_Chl	C:Chl	DIA:50[b] LND:100[b] SNP-PRO:300[b]	mg/mg
μ_{max}	Maximal growth rate	DIA:5[b] LND:4[b] SNP-PRO:2.8[b]	day^{-1}
k_{par}	PAR saturation coefficient (mean-std)	DIA-LND:0.004–0.003[c] SNP-PRO:0.012–0.01[a-b]	(µEin·m^{-2}·s^{-1})$^{-1}$
κ_{PO4}	PO$_4$ half-saturation constant	DIA-LND:0.05–0.07[c] SNP:0.015–0.035[a-b] PRO:0.005–0.010[d]	mmolP·m^{-3}
κ_{NH4}	NH$_4$ half-saturation constant	DIA-LND:0.4–0.56[c] SNP:0.12–0.28[a-b] PRO:0.04–0.08[d]	mmolN·m^{-3}
κ_{NO2}	NO$_2$ half-saturation constant	DIA-LND:0.8–1.12[c] SNP:0.24–0.56[a-b] PRO:0.08–0.16[d]	mmolN·m^{-3}
κ_{NO3}	NO$_3$ half-saturation constant	DIA-LND:0.8–1.12 SNP:0.24–0.56[a-b]	mmolN·m^{-3}
κ_{Si}	Si half-saturation constant	DIA:1[b]	mmolSi·m^{-3}
k_{inhib}	PAR inhibition coefficient (mean-std)	1.10^{-3}–5.10^{-5} [a-b-c]	(µEin·m^{-2}·s^{-1})$^{-1}$
T_{opt}	Phytoplankton temperature optimum (min-max)	5–25[c]	°C
A	Phytoplankton temperature coefficient A	1.04[a-b]	

Table A1 (*continued*)

Param	Signification	Value	Unit
B	Phytoplankton temperature coefficient B	0.001[a-b-c]	°C^{-1}
T_{power}	Temperature exponent	4[a-b]	
T_{norm}	Temperature normalisation coefficient	0.3[a-b]	
T_{coef}	Temperature normalisation coefficient	0.33[a-b]	
palat(z_1,j)	Microzooplankton palatability	DIA:0.28[a] LND:0.4[a] SNP-PRO:1[a]	
palat(z_2,j)	Mesozooplankton palatability	DIA:0.7[a] LND:1[a] SNP-PRO:0.2[a] Microzoo:1[a]	
ExportFracP	Fraction of phytoplankton mortality exported as particulate matter	DIA-LND:50[a-b] SNP-PRO:20[a-b]	%
K_{pPOP}	POP remineralisation rate	0.033[a-b]	day^{-1}
K_{pPON}	PON remineralisation rate	0.033[a-b]	day^{-1}
K_{pPOSi}	POSi remineralisation rate	0.0033[a-b]	day^{-1}
K_{dDOP}	DOP remineralisation rate	0.2[d]	day^{-1}
K_{dDON}	DON remineralisation rate	0.2[d]	day^{-1}
$Knit_{NO2}$	Nitritation rate	0.1[a-b]	day^{-1}
$Knit_{NO3}$	Nitratation rate	0.033[a-b]	day^{-1}
SinkPOP	POP sinking rate	10[a-b]	m·day^{-1}
SinkPON	PON sinking rate	10[a-b]	m·day^{-1}
SinkPOSi	POSi sinking rate	10[a-b]	m·day^{-1}
sigma	NO$_x$ uptake inhibition by NH$_4$	4.6[a-b]	mmolSi·m^{-3}
mortp	Phytoplankton mortality rate	0.1[a-b]	day^{-1}
assef(z_1,j)	Phytoplankton assimilation efficiency for microzooplankton	30[c]	%
assef(z_2,j)	Phytoplankton assimilation efficiency for mesozooplankton	30[c]	%
grazemax	Maximal grazing rate	Z_1:1.5[d] Z_2:0.5[a]	day^{-1}
ksatgraz	Grazing half-saturation constant	0.07[c]	mmolP·m^{-3}
mortz	Linear mortality rate	Z_1:0.033[a-b] Z_2:0.001[d]	day^{-1}
mortquadz	Mesozooplankton quadratic mortality rate	0.01 ∗ Z_2 / 0.01[d]	day^{-1}
assefzoo	Assimilation efficiency of microzooplankton for mesozooplankton	30[a-b]	%
ExportFracGraz	Sloppy-feeding exported as particulate matter	80[a]	%
ExportFracZ	Mortality exported as particulate matter	Z_1:20[a] Z_2:70[a]	%

References

Brun, P., Vogt, M., Payne, M.R., Gruber, N., O'Brien, C.J., Buitenhuis, E.T., Le Quéré, C., Leblanc, K., Luo, Y.W., 2015. Ecological niches of open ocean phytoplankton taxa. Limnol. Oceanogr. 60 (3), 1020–1038.

Cadier M., Sourisseau M., Gorgues, T. Edwards, C.A., Memery, L., Assessing spatial and temporal variability of phytoplankton communities' composition in the Iroise Sea ecosystem (Brittany, France) : a 3D modeling approach. Part 2 : Linking mesoscale distribution of phenotypic diversity to hydrodynamism. submitted to Journal of Marine Systems.

Cambon, G., 2008. Etude numérique de mer d'Iroise: dynamique, variabilité de front d'Ouessant et evaluation des échanges cross-frontaux. Université de Bretagne Occidentale, Brest, France (195 pp.).

Casotti, R., Landolfi, A., Brunet, C., D'Ortenzio, F., Mangoni, O., Ribera d'Alcalà, M., Denis, M., 2003. Composition and dynamics of the phytoplankton of the Ionian Sea (eastern Mediterranean). J. Geophys. Res. Oceans 108 (C9), 1978–2012.

Chan, A.T., 1978. Comparative physiological study of marine diatoms and dinoflagellates in relation to irradiance and cell size. I: growth under continuous light. J. Phycol. 14 (4), 396–402.

Chan, A.T., 1980. Comparative physiological study of marine diatoms and dinoflagellates in relation to irradiance and cell size. II: relationship between photosynthesis, growth and carbon/chlorophyll a ratio. J. Phycol. 16, 428–432.

Chen, B., Liu, H., 2010. Relationships between phytoplankton growth and cell size in surface oceans: interactive effects of temperature, nutrients, and grazing. Limnol. Oceanogr. 55 (3), 965.

Chesson, P., 2000. Mechanisms of maintenance of species diversity. Annu. Rev. Ecol. Syst. 31.

Dutkiewicz, S., Follows, M.J., Bragg, J.G., 2009. Modeling the coupling of ocean ecology and biogeochemistry. Glob. Biogeochem. Cycles 23.

Edwards, A.M., Yool, A., 2000. The role of higher predation in plankton population models. J. Plankton Res. 22 (6), 1085–1112.

Edwards, K.F., Thomas, M.K., Klausmeier, C.A., Litchman, E., 2015. Light and growth in marine phytoplankton: allometric, taxonomic, and environmental variation. Limnol. Oceanogr. 60, 540–552.

Eppley, R.W., Thomas, W.H., 1969. Comparison of half-saturation constants for growth and nitrate uptake of marine phytoplankton 2. J. Phycol. 5 (4), 375–379.

Falkowski, P.G., Raven, J.A., 1997. Aquatic Photosynthesis. Blackwell Science, Malden, MA.

Finkel, Z.V., 2001. Light absorption and size scaling of light-limited metabolism in marine diatoms. Limnol. Oceanogr. 46 (1), 86–94.

Flynn, K.J., Stoecker, D.K., Mitra, A., Raven, J.A., Glibert, P.M., Hansen, P.J., Graneli, E., Burkholder, J.M., 2012. Misuse of the phytoplankton-zooplankton dichotomy: the need to assign organisms as mixotrophs within plankton functional types. J. Plankton Res. 35, 3–11.

Follows, M.J., Dutkiewicz, S., Grant, S., Chisholm, S.W., 2007. Emergent biogeography of microbial communities in a model ocean. Science 315, 1843–1846.

Franks, P.J.S., 1992. Sink or swim: accumulation of biomass at fronts. Mar. Ecol. Prog. Ser. 82, 1–12.

Furnas, M.J., 1990. In-situ growth rates of marine phytoplankton: approaches to measurement, community and species growth rates. J. Plankton Res. 12, 1117–1151.

Gan, G., Ma, C., Wu, J., 2007. Data Clustering: Theory, Algorithms, and Applications (Siam).

Geider, R.J., 1987. Light and temperature dependence of the carbon to chlorophyll a ratio in microalgae and cyanobacteria: implications for physiology and growth of phytoplankton. New Phytol. 106 (1), 1–34.

Geider, R.J., MacIntyre, H.L., Kana, T.M., 1997. Dynamic model of phytoplankton growth and acclimation: responses of the balanced growth rate and the chlorophyll a: carbon ratio to light, nutrient-limitation and temperature. Mar. Ecol. Prog. Ser. 148, 187–200.

Glover, H.E., Keller, M.D., Spinard, R.W., 1987. The effects of light quality and intensity on photosynthesis and growth of marine eukaryotic and prokaryotic phytoplankton clones. Journal of Marine Biology and Ecology 105, 137–159.

Goebel, N.L., Edwards, C.A., Zehr, J.P., Follows, M.J., 2010. An emergent community ecosystem model applied to the California Current System. J. Mar. Syst. 83, 221–241.

Gohin, F., Druon, J.N., Lampert, L., 2002. A five channel chlorophyll concentration algorithm applied to SeaWiFS data processed by SeaDAS in coastal waters. Int. J. Remote Sens. 23, 1639–1661.

Gohin, F., Saulquin, B., Oger-Jeanneret, H., Lozac'h, L., Lampert, L., Lefebvre, A., Riou, P., Bruchon, F., 2008. Towards a better assessment of the ecological status of coastal waters using satellite-derived chlorophyll-a concentrations. Remote Sens. Environ. 112, 3329–3340.

Hansen, B.W., Bjørnsen, P.K., Hansen, B.W., 1997. Zooplankton grazing and growth: scaling within the 2–2,000-~ III body size range. Limnol. Oceanogr. 42, 687–704.

Harrison, W.G., Platt, T., 1986. Photosynthesis-irradiance relationships in polar and temperate phytoplankton populations. Polar Biol. 5, 153–164.

Holligan, P.M., Williams, P.J.L., Purdie, D., Harris, R.P., 1984. Photosynthesis, respiration and nitrogen supply of plankton populations in stratified, frontal and tidally mixed shelf waters. Mar. Ecol. Prog. Ser. 17, 201–213.

Huisman, J., Sharples, J., Stroom, J.M., Visser, P.M., Kardinaal, E.A., Verspagen, M.H., Sommeijer, B., 2004. Changes in turbulent mixing shift competition for light between phytoplankton species. Ecology 85, 2960–2970.

Hutchinson, G.E., 1961. The paradox of the plankton. Am. Nat. 95, 137–145.

Irwin, A.J., Finkel, Z.V., Schofield, O.M., Falkowski, P.G., 2006. Scaling-up from nutrient physiology to the size-structure of phytoplankton communities. J. Plankton Res. 28 (5), 459–471.

Jain, A.K., Murty, M.N., Flynn, P.J., 1999. Data clustering: a review. ACM Computing Surveys (CSUR). 31. pp. 264–323.

Jiang, G.-S., Shu, C.-W., 1996. Efficient implementation of weighted ENO schemes. J. Comput. Phys. 126, 202–228.

Johnson, Z.I., Zinser, E.R., Coe, A., McNulty, N.P., Malcolm, E., Woodward, S., Chisholm, S.W., 2006. Niche Partitioning Among Prochlorococcus Ecotypes Along Ocean-Scale Environmental Gradients Science. 311 pp. 1737–1740.

Kaufman, L., Rousseeuw, P.J., 1990. Partitioning Around Medoids (Program Pam). Finding Groups in Data: An Introduction to Cluster Analysis. pp. 68–125.

Klausmeier, C.A., Litchman, E., Levin, S.A., 2007. A model of flexible uptake of two essential resources. J. Theor. Biol. 246 (2), 278–289.

Landeira, J.M., Ferron, B., Lunven, M., Morin, P., Marié, L., Sourisseau, M., 2014. Biophysical interactions control the size and abundance of large phytoplankton chains at the Ushant tidal front. PLoS One 9, e90507.

Large, W.G., McWilliams, J.C., Doney, S.C., 1994. Oceanic vertical mixing: a review and a model with a nonlocal boundary layer parameterization. Review in Geophysics. 32, pp. 363–403.

Le Boyer, A., Cambon, G., Daniault, N., Herbette, S., Le Cann, B., Marié, L., Morin, P., 2009. Observations of the Ushant tidal front in September 2007. Cont. Shelf Res. 29, 1026–1037.

Le Corre, P., L'Helguen, S., 1993. Nitrogen source for uptake by Gyrodinium cf. aureolum in a tidal front. Limnol. Oceanogr. 38, 446–451.

Le Fèvre, J., Grall, J.R., 1970. On the relationships of Noctiluca swarming off the western coast of brittany with hydrological features and plankton characteristics of the environment. J. Exp. Mar. Biol. Ecol. 4, 287–306.

Le Fèvre, J., Viollier, M., Le Corre, P., Dupouy, C., Grall, J.R., 1983. Remote sensing observations of biological material by LANDSAT along a tidal thermal front and their relevancy to the available field data. Estuar. Coast. Shelf Sci. 16, 37–50.

Le Pape, O., Jean, F., Ménesguen, A., 1999. Pelagic and benthic trophic chain coupling in a semi-enclosed coastal system, the Bay of Brest (France): a modelling approach. Mar. Ecol. Prog. Ser. 189, 135–147.

Legendre, L., Robineau, B., Leblanc, B., 1999. Single-celled cyanobacteria in the first-year sea ice and ice-covered waters of the Northern Hemisphere. Bull. Inst. Oceanogr. 169–174.

Litchman, E., Klausmeier, C.A., Schofield, O.M., Falkowski, P.G., 2007. The role of functional traits and trade-offs in structuring phytoplankton communities: scaling from cellular to ecosystem level. Ecol. Lett. 10, 1170–1181.

Liu, W.T., Katsaros, K.B., Busiger, J.A., 1979. Bulk parametrization of air-sea exchanges of heat and water vapor including the molecular constraints at the interface. J. Atmos. Sci. 36 (1922-1735).

Liu, X.-D., Osher, S., Chan, T., 1994. Weighted essentially non-oscillatory schemes. J. Comput. Phys. 115, 200–212.

MacIntyre, H.L., Kana, T.M., Anning, T., Geider, R.J., 2002. Photoacclimation of photosynthesis irradiance response curves and photosynthetic pigments in microalgae and cyanobacteria. J. Phycol. 38, 17–38.

Maguer, J.-F., L'Helguen, S., Caradec, J., Klein, C., 2011. Size-dependent uptake of nitrate and ammonium as a function of light in well-mixed temperate coastal waters. Cont. Shelf Res. 31, 1620–1631.

Marañon, E., Cermeno, P., López-Sandoval, D.C., Rodríguez-Ramos, T., Sobrino, C., Huete-Ortega, M., Blanco, J.M., Rodriguez, J., 2013. Unimodal size scaling of phytoplankton growth and the size dependence of nutrient uptake and use. Ecol. Lett. 16 (3), 371–379.

Margalef, R., 1978. Life-forms of phytoplankton as survival alternatives in an unstable environment. Oceanol. Acta 1, 493–509.

Marie, D., Brussaard, C., Partensky, F., Vaulot, D., Wiley, J., 1999. Flow cytometric analysis of phytoplankton, bacteria and viruses. Curr. Protoc. Cytom. 11, 1–15.

Mariette, V., Le Cann, B., 1985. Simulation of the formation of Ushant thermal front. Cont. Shelf Res. 4, 637–660.

Mariette, V., Rougier, G., Salomon, J.C., Simon, B., 1982. Courants de marée et mer d'Iroise. Oceanol. Acta 5, 149–160.

Mitra, A., Flynn, K.J., 2010. Modelling mixotrophy in harmful algal blooms: more or less the sum of the parts? J. Mar. Syst. 83, 158–169.

Moore, L.R., Post, A.F., Rocap, G., Chisholm, S.W., 2002. Utilization of different nitrogen sources by the marine cyanobacteria Prochlorococcus and Synechococcus. Limnol. Oceanogr. 47 (4), 989–996.

Olson, R.J., Chisholm, S.W., Zettler, E.R., Altabet, M.A., Dusenberry, J.A., 1990. Spatial and temporal distributions of prochlorophyte picoplankton in the North Atlantic Ocean. Deep Sea Res. Part A 37, 1033–1051.

Osmond, C., Valaane, N., Haslam, S., Votila, P., 1995. An empirical model of the phytoplankton chlorophyll: carbon ratio-the conversion factor between productivity and growth rate. Can. J. Fish. Aquat. Sci. 43, 788–796.

Pairaud, I.L., Auclair, F., Marsaleix, P., Lyard, F., Pichon, A., 2008a. Dynamics of the semi-diurnal and quarter-diurnal internal tides in the Bay of Biscay. Part 2: baroclinic tides. Cont. Shelf Res. 30, 253–269.

Pairaud, I.L., Lyard, F., Auclair, F., Letellier, T., Marsaleix, P., 2008b. Dynamics of the semi-diurnal and quarter-diurnal internal tides in the Bay of Biscay. Part 1: barotropic tides. Cont. Shelf Res. 28, 1294–1315.

Partensky, F., Hess, W.R., Vaulot, D., 1999. Prochlorococcus, a Marine Photosynthetic Prokaryote of Global Significance Microbiology and Molecular Biology Reviews. 63 pp. 106–127.

Penven, P., Debreu, L., Marchesiello, P., McWilliams, J.C., 2006. Evaluation and application of the ROMS 1-way embedding procedure to the Central California upwelling system. Ocean Model 12, 157–187.

Pingree, R.D., 1978. Cyclonic eddies and cross-frontal mixing. J. Mar. Biol. Assoc. UK 58, 955–963.

Pingree, R.D., Holligan, P.M., Mardell, G.T., 1978. The effects of vertical stability on phytoplankton distributions in the summer on the northwest European shelf. Deep-Sea Res. 25, 1011–1028.

Raven, A., Finkel, Z.V., Irwin, A.J., 2005. Picophytoplankton: bottom-up and top-down controls on ecology and evolution. Vie et Milieu 55 (3–4), 209–216.

Rees, A.P., Joint, I.R., Donald, K.M., 1999. Early spring bloom phytoplankton-nutrient dynamics at the Celtic Sea Shelf Edge. Deep-Sea Res. I 46, 483–510.

Schultes, S., Sourisseau, M., Le Masson, E., Lunven, M., Marié, L., 2013. Influence of physical forcing on mesozooplankton communities at the Ushant tidal front. J. Mar. Syst. 109-110, S191–S202.

Shchepetkin, A.F., McWilliams, J.C., 2005. The regional oceanic modeling system (ROMS): a split-explicit, free-surface, topography-following-coordinate oceanic model. Ocean Model 9, 347–404.

Sournia, A., Brylinski, J.-M., Dallot, S., Le Corre, P., Leveau, M., Prieur, L., Froget, C., 1990. Fronts hydrologiques au large des côtes françaises: Les sites ateliers du programme Frontal. Oceanol. Acta 13, 413–438.

Straile, D., 1997. Gross growth efficiencies of protozoan and metazoan zooplankton and their dependence on food concentration, predator-prey weight ratio, and taxonomic group. Limnol. Oceanogr. 42 (6), 1375–1385.

Suzuki, K., Handa, N., Kiyosawa, H., Ishizaka, J., 2003. Distribution of the prochlorophyte Prochlorococcus in the Central Pacific Ocean as measured by HPLC. Limnol. Oceanogr. 40, 983–989.

Sverdrup, H.U., 1953. On conditions for the vernal blooming of phytoplankton. J. Conseil. 18, 287–295.

Tilman, D., 1987. On the meaning of competition and the mechanisms of competitive superiority. Funct. Ecol. 304–315.

Vallina, S.M., Ward, B.A., Dutkiewicz, S., Follows, M.J., 2014. Maximal feeding with active prey-switching: a kill-the-winner functional response and its effect on global diversity and biogeography. Prog. Oceanogr. 120, 93–109.

Verity, P.G., Robertson, C.Y., Tronzo, C.R., Anderws, M.G., Nelson, J.R., Sieracki, M.E., 1992. Relationships between cell volume and the carbon and nitrogen content of marine photosynthetic nanoplankton. Limnol. Oceanogr. 37, 1434–1446.

Videau, C., 1987. Primary production and physiological state of phytoplankton at the Ushant tidal front (west coast of Brittany, France). Mar. Ecol. Prog. Ser. 35, 141–151.

Zubkov, M.V., Sleigh, M.A., Burkill, P.H., 2000. Assaying picoplankton distribution by flow cytometry of underway samples collected along a meridional transect across the Atlantic Ocean. Aquat. Microb. Ecol. 21, 13–20.